

# Hydrodynamics and Conjugate Mass Transfer Through the Interface of a Translating Spherical Droplet

Azeddine Rachih, S. Charton, Dominique Legendre, Éric Climent

▶ **To cite this version:**

Azeddine Rachih, S. Charton, Dominique Legendre, Éric Climent. Hydrodynamics and Conjugate Mass Transfer Through the Interface of a Translating Spherical Droplet. AIChE Annual Meeting, Oct 2018, Pittsburgh, United States. cea-02339863

**HAL Id: cea-02339863**

**https://cea.hal.science/cea-02339863**

Submitted on 17 Mar 2020

**HAL** is a multi-disciplinary open access archive for the deposit and dissemination of scientific research documents, whether they are published or not. The documents may come from teaching and research institutions in France or abroad, or from public or private research centers.

L'archive ouverte pluridisciplinaire **HAL**, est destinée au dépôt et à la diffusion de documents scientifiques de niveau recherche, publiés ou non, émanant des établissements d'enseignement et de recherche français ou étrangers, des laboratoires publics ou privés.

# Hydrodynamics and Conjugate Mass Transfer Through the Interface of a Translating Spherical Droplet

Azeddine Rachih[a,b,*], Sophie Charton[a], Dominique Legendre[b], Eric Climent[b]

[a] *CEA, DEN, Research Department on Mining and Fuel Recycling, SA2I, F-30207 Bagnols-sur-Cèze, France*

[b] *Institut de Mécanique des Fluides de Toulouse (IMFT), Université de Toulouse, CNRS, Toulouse France*

**Abstract**

A numerical investigation has been conducted by DNS to investigate the coupling between the internal and the external flows and their respective effects on mass transfer from a translating droplet in an immiscible phase. Low to moderate Reynolds flows have been investigated $0.1 < Re < 100$. On the first part of this paper, efforts have been made to suggest new correlations of the drag coefficient and the angle of separation angle in terms of $Re$ and the viscosity ratio $\mu^*$. In the second part, computations were focused on flow parameters influence on the conjugate mass transfer and especially the evolution of the Sherwood number. The results has been compared with available experimental and numerical data. Moreover, through a parametric study, the effect of relevant physical parameters on the transfer process is investigated. An interesting behavior $Sh$ is evidenced for low Henry coefficient in a convective dominant process.

*Keywords:* Droplet hydrodynamics, Multiphase flow, Sherwood number, Interfacial phenomena

## 1. Introduction

In solvent extraction process, regardless of the type of contactors, the contact area between the two non-miscible liquid phases is enhanced by dispersing one of the liquid phases as droplets into the other (continuous) one. The solute transfer direction depends primarily on the solute gradient and the chemical affinity in both phases. The inter-phase mass transfer occurs inherently at the boundaries of the droplets. Thus, the flow-field and mass transfer in droplet swarms are essential for the design of liquid-liquid extraction devices. In order to capture these complex phenomena properly, the case of a single droplet has to be considered first.

*Corresponding author

*Email address:* azeddine.rachih@imft.fr (Azeddine Rachih )

Mass transfer to/from a translating drop in an immiscible and quiescent liquid has been widely investigated, both experimentally and numerically for typical liquid-liquid systems encountered in solvent extraction [31]. The single droplet problem is intrinsically a complex and multi-variable problem, as in most operational conditions, depending on their size and relative velocity, droplets can be seen either as rigid entities, or as circulating where internal circulations, triggered by the external flow, might develop. These circulation patterns are likely to move the inner mass transfer mechanism from a purely diffusive one, to an advective–diffusive process ([13], [12]), where the solute distribution depends not only on the concentration gradient but also on the droplet hydrodynamics. A coupling between the mass transfer and the hydrodynamics is hence established, making the problem's physics sensitive to most of the system parameters such as viscosity ratio, mass diffusivity ratio, etc.

The first comprehensive study of droplet hydrodynamics is undoubtedly the reference book by Clift et al. [5], where the shape of the drop (spherical, or deformed or oscillating) depending on the relative values of the Reynolds, Eötvös and Morton numbers is particularly discussed. In the case of a fully mobile interface (i.e. a complete absence of impurities or surfactants), one can spot the droplet's shape on the Clift diagram (Page 27 in [5]) giving these three dimensionless parameters. It allows moreover to calculate the terminal velocity of the droplet in a quiescent liquid.

Regarding the mass transfer problem as for the heat transfer ones, three distinct behaviours are distinguished depending on where the main mass transfer resistance resides. They are generally referred to as : internal problem (when the main resistance is located in the particle), external problem (main resistance outside) and conjugate problem (comparable resistances) respectively. The main difference between the heat and mass transfer cases resides in the interface conditions. Indeed, while in thermal problem the temperature is the same on both sides of the interface, a concentration step generally prevails regarding the transferred species, which value, in non reactive system, is given by thermodynamic equilibrium. If $k$ denotes the Henry coefficient, and $D^c$ and $D^d$ the solute diffusivity coefficients in the continuous phase and in the droplet phase respectively, the mass transfer regime can be assessed by the value of the quantity $k\sqrt{D^d/D^c}$ [32]. Hence, if $k\sqrt{D^d/D^c} << 1$ the problem is supposed to be internal, it is considered external when $k\sqrt{D^d/D^c} >> 1$, and a conjugate problem when $k\sqrt{D^d/D^c} \approx 1$.

The solution of the internal problems, where the stream flow imposes the concentration value at the interface, was first derived analytically by Newman [20]. For this problem controlled by pure diffusion ($Pe/(\mu^* + 1) \longrightarrow 0$) in a spherical droplet, the author shows that the asymptotic value of the Sherwood number converges toward $Sh_{Newman} = 6.58$. Later, Kronig and Brink [16] considered the case of a circulating droplet in a creeping flow, with $Pe/(\mu^* + 1) \longrightarrow \infty$ and highlighted a second asymptotic value of the Sherwood number $Sh_{Kronig} = 17.9$. In all other configurations however, finding an analytical solution is less straightforward and a numerical approach is required. Hence, for intermediate Peclet

numbers, numerical simulations by resolving the mass transport equation in a Hadamard-Rybczynski solution were proposed by (Juncu [12], Brignell [4], Wylock et al. [32]). At intermediate Reynolds numbers, Colombet et al. [6] addressed the case of a small viscosity ratio($\mu^* = 0.018$). The simulation of both the internal and external flows was first solved by Uribe-Ramirez and Korchinsky [30] using the weighted residuals method [10]), but Ubal et al. [29] later evidenced some limitations of the boundary layer model they proposed.

Regarding the external problems, the concentration is uniform inside the droplet and along the interface. However the value of the drop concentration may vary with time. Most of the studies labelled as external mass/heat transfer consider a constant concentration at the interface which might be sometimes misleading. Abramzon and Fishbein [2] addressed numerically the solution of the convection-diffusion equation for a solute transferred from a droplet in a creeping flow for Peclet numbers $Pe < 1000$. The same authors also considered the transient heat transfer problem in a Stokes flow, in a rather large range of Peclet number $1 < Pe < 10000$ [1]. Many numerical studies were proposed for intermediated Reynolds flows (see e.g. Saboni et al. [28] , Alexandrova et al. [3], Feng and Michaelides [9]), and correlations of mass transfer coefficient have been proposed by Feng and Michaelides [9]. A review of the main correlations for internal and external problems in circulating drops are summarized by Kumar and Hartland [17].

While the internal/external problems have been heavily studied, the solution of the conjugate problems is still an active area of research. This type of problems involves taking into account the concentration in both the continuous and the dispersed phases. As mentioned previously, one particularity is that the interfacial concentration is ruled by both an equilibrium law (as the Henry law) and the continuity of mass flux. In creeping flow, Ruckenstein [27] derived an interesting analytical equation for the Sherwood number using similarity variables in the case of creeping flow. Cooper [7] had found an analytical solution for the conjugate transfer at low Peclet. Still in creeping flows, Oliver and Chung [23] considered the heat transfer from a translating droplet. The transient diffusive convective heat equation is solved in a flow field governed by the Hadamard-Rybczynski equation. The effect of the volumetric heat capacities ratio was illustrated for different Peclet numbers. A similar configuration was considered by Kleinman and Reed [15] for mass transfer where the parametric study moreover considered the influence of the Henry coefficient. The addition rule has been proven not accurate enough, a correction was proposed by the authors. A more general sensitivity study of the temporal evolution of the Sherwood number was proposed by Paschedag et al. [24].

The paper is organized as follows. The numerical procedure is described in Section 2 where the governing equations, the typical conditions at the interface, the mesh features are successively discussed. Section 3.2 where the predicted fluid motion, internal and the external transfer rates are compared to available analytical or numerical data based on the previously produced case studies. Finally, thanks to the general model developed, a complete study of the problem of conjugate mass transfer is proposed in Sec 4, where the sensibility

to the main parameters ($\mu^*$, $\rho^*$, $D^*$, $k$) is studied and analysed.

## 2. Model description

### *2.1. General*

The flow around and inside a spherical droplet, with a prescribed and fixed shape is investigated by direct numerical simulation (DNS).
In this study, the external flow is assumed to be uniform. The two liquid phases are considered Newtonian, and incompressible. The non deformable interface is supposed to be completely free from surface-active contaminants. Meaning that the continuity of the velocity and of the tangential shear stress have to be fulfilled at the interface (no possible Marangoni effects due to surface tension variations). By convention, the mass transfer rate is assumed to occur from the droplet (with a given initial solute concentration) to the external fluid. In addition, we assume that the density and the viscosity of the two phases are not affected by the changes in the solute. With these assumptions, the continuity and the momentum transport equations can be solved separately from the mass transport equations.

The numerical model is based on the balance equations written in dimensionless form in an inertial reference frame attached to the center of mass of the droplet. A two-dimensional axisymmetric computational domain is used. The latter is divided into two distinct subdomains: one referred to the droplet phase and the other one represents the continuous phase. The droplet radius, $R$ is used as the length reference. Similarly, the free stream velocity $U_0$ is used as the velocity scale. The global size of the computational domain is approximately $50R$.

### *2.2. Governing equations*

The flow fields are computed by solving the unstationary incompressible Navier–Stokes and continuity equations in both phases, in a general orthogonal curvilinear coordinates $(\xi_i)_{i=1,3}$ as recommended by Magnaudet et al. [18].
$\mathbf{V}^\delta$ stands for the dimensionless velocity along the coordinate line $\xi_i'$ and the physical length $\xi_i' = h_i d\xi_i$ (where $h_i$ denotes the factor scale along the direction $i$), $P^\delta$ represents the dimensionless pressure. The superscript $\delta$ refers to either the dispersed phase "d" or the continuous phase "c". The Navier-Stokes equations can be written in each phase "$\delta$" in the dimensionless and compact conservative form (Pope [25]) :

$$\begin{aligned} &\frac{\partial V_j^\delta}{\partial \xi_j} = 0 \\ &\frac{\partial V_i^\delta}{\partial t} + \frac{\partial \left(V_i^\delta V_j^\delta\right)}{\partial \xi_j} = -\frac{\partial P^\delta}{\partial \xi_i} + \frac{\partial \left(\tau_{ij}^\delta\right)}{\partial \xi_j} + H_j^i \left(V_j^\delta V_j^\delta - \tau_{jj}^\delta\right) - H_j^i \left(V_i^\delta V_j^\delta - \tau_{ij}^\delta\right) \end{aligned} \tag{1}$$

The stretching factors (curvature terms) $H_j^i$ are defined as :

$$H_j^i = \frac{1}{h_j}\frac{\partial h_j}{\partial \xi_i} \tag{2}$$

$\tau_{ij}^{\delta}$ represents the dimensionless components of the viscous stress given in the considered orthogonal curvilinear coordinates by :

$$\begin{aligned} \tau_{ij}^{d} &= \frac{1}{Re}\left[\frac{\partial V_i^d}{\partial \xi_j} + \frac{\partial V_j^d}{\partial \xi_i} - H_j^i V_j^d - H_i^j V_i^d + 2H_i^k V_k^d \delta_{i,j}\right] \\ \tau_{ij}^{c} &= \frac{\mu^*}{Re}\left[\frac{\partial V_i^c}{\partial \xi_j} + \frac{\partial V_j^c}{\partial \xi_i} - H_j^i V_j^c - H_i^j V_i^c + 2H_i^k V_k^c \delta_{i,j}\right] \end{aligned} \tag{3}$$

$\mu^*$ is the ratio of the dynamic viscosities ($\mu^d/\mu^c$). The Reynolds number shown in the $\tau_{ij}^{\delta}$ expression is defined by $Re = \frac{U_0 2R}{\nu^c}$, with $\nu^c$ denotes the kinematic viscosity of the continuous phase.

The mass transfer resistance is considered to be comparable in both phases. Hence the inner and outer concentration fields are computed by solving the transient mass transport equations in both phases. The dimensionless concentration of the solute in phase "$\delta$", it is defined as $C^{\delta} = \dfrac{C'^{\delta} - C'_{\infty}}{C'^{d}_0 - C'_{\infty}}$ (the prime refers to dimensional concentration) where $C'^{d}_0$ stands for the initial concentration inside the droplet and $C'_{\infty}$ for the solute concentration in the stream flow, far from the droplet. In the absence of chemical reaction, the mass balance equation involves only convective and diffusive transport terms. In the considered coordinates system ($\xi_i$) the dimensionless solute's balance equations read :

$$\begin{aligned} \frac{\partial C^d}{\partial t} + \frac{\partial\left(V_j^d C^d\right)}{\partial \xi_j} &= \frac{1}{Pe}\frac{\partial^2 C^d}{\partial \xi_j^2} \\ \frac{\partial C^c}{\partial t} + \frac{\partial\left(V_j^c C^c\right)}{\partial \xi_j} &= \frac{D^*}{Pe}\frac{\partial^2 C^c}{\partial \xi_j^2} \end{aligned} \tag{4}$$

$Pe = \frac{2U_0 R}{D^c}$ is the external Peclet number. Note that $Pe$ is the product of the Reynolds number and the Schmidt number $Sc = \frac{\nu^c}{D^c}$, with $D^c$ the solute's mass diffusivity in the continuous phase.

### *2.3. Interface conditions*

The droplet interface is considered to be free from surface-active contaminants. Hence the tangential velocity and shear stress are continuous at the interface while the velocity normal component at the interface is equal to 0. Moreover, since the spherical droplet is

non-deformable, there is no need to specify a condition for the normal stress at the interface. Therefore, the hydrodynamic jump conditions at the interface are expressed as follow, where $(\mathbf{n}, \mathbf{t})$ are the normal and the tangential vectors to the interface respectively :

$$\begin{aligned} \mathbf{V^d} \cdot \mathbf{t} &= \mathbf{V^c} \cdot \mathbf{t} \\ \mathbf{V^d} \cdot \mathbf{n} &= \mathbf{V^c} \cdot \mathbf{n} = 0 \\ (\boldsymbol{\tau}_\mathbf{I}^\mathbf{d} \cdot \mathbf{n}) \cdot \mathbf{t} &= (\boldsymbol{\tau}_\mathbf{I}^\mathbf{c} \cdot \mathbf{n}) \cdot \mathbf{t} \end{aligned} \tag{5}$$

Regarding the transferred species, equilibrium distribution is assumed to prevail at the droplet's interface. Besides, as the mass flux at the interface is continuous, therefore the mass jump conditions at the interface may be expressed in by the following equations :

$$\begin{aligned} C_I^d &= k \cdot C_I^c \\ -\frac{D^d}{D^c} \frac{\partial C^d}{\partial \mathbf{n}} \bigg|_I &= -\frac{\partial C^c}{\partial \mathbf{n}} \bigg|_I \end{aligned} \tag{6}$$

Where $k$ is the distribution coefficient or sometimes called the Henry coefficient (namely in liquid-gas systems).

*2.4. Meshing & Discretization*

Two types of orthogonal curvilinear meshes have been considered in this study. In both cases the droplet is discretized using a polar mesh centred at the droplet center. Whereas for the continuous phase domain, two meshing strategies have been proposed. The first mesh is based on the streamlines $\psi$ and the equipotential lines of a potential flow around a cylinder. The expressions of $\Psi$ and $\phi$ in the considered polar coordinates are :

$$\begin{cases} \phi = \xi_1 = -\cos(\theta) \left(r + R^2/r\right) \\ \psi = \xi_2 = -\sin(\theta) \left(1 - R^2/r^2\right) \end{cases} \tag{7}$$

It is important to note that $\psi$ and $\phi$ are orthogonal by definition. In the second approach, as for the droplet, a polar mesh is used for the continuous phase domain. In each case, the mesh is axisymmetric and presents a bijection with the Cartesian coordinates.

The Navier Stokes and the diffusion-convective transport equation are solved using a staggered mesh where the pressure nodes and the velocity nodes are shifted from one another. The second order discretization of the jump conditions at the interface are given by Equations (8)- (11) illustrated in Figure 1. These expressions, where the ratios of the relevant phase properties are highlighted is red, enable to link the internal/external hydrodynamics and the mass transfer. The discretization factors of Eq (8)- (11) are detailed in Appendix A.

The studied meshes are presented in Figure 2. and their corresponding numerical domains in Figure 3. A refining at the interface is necessary in order to resolve both the hydrodynamic and the mass boundary layer with a good precision. The thickness of this later can be approximated by $R/Re^{1/2}$ for the hydrodynamic boundary layer and $R/Pe^{1/2}$ for the mass boundary layer.

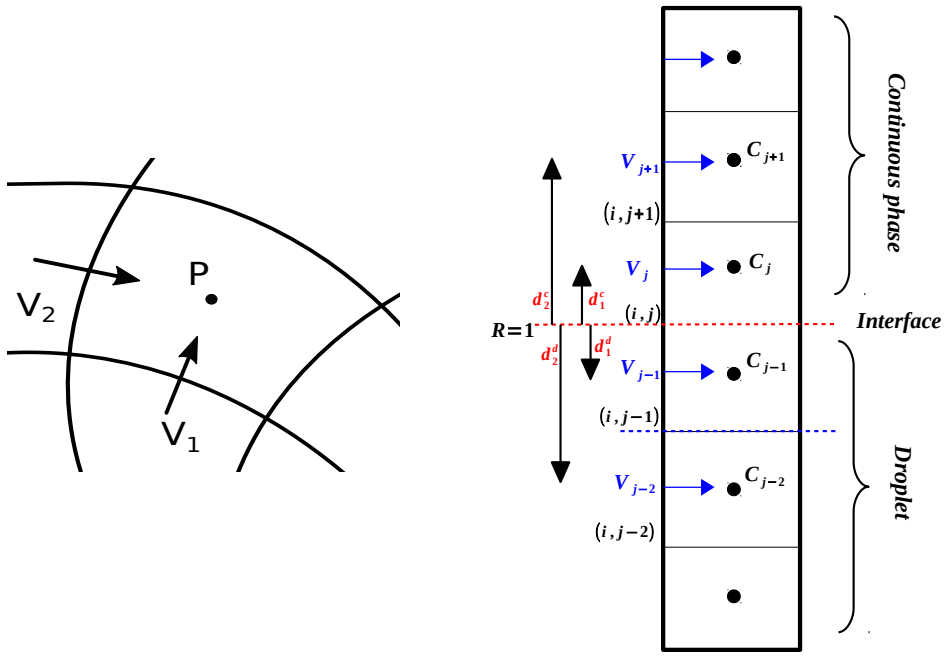



Figure 1: Left : General scheme of a calculation cell, Right : Discretization at the interface

$$(\boldsymbol{\tau}_{\mathbf{I}}^{\mathbf{c}} \cdot \mathbf{n}) \cdot \mathbf{t} = \frac{\mu^d}{\mu^c} \frac{d3v^d\, V_{j-2}^d - d2v^d V_{j-1}^d + \dfrac{(d1v^d - H_2^1)(d2v^c\, V_j^c - d3v^c\, V_{j+1}^c)}{d1v^c + H_2^1}}{1 + \dfrac{\mu^d}{\mu^c} \dfrac{d1v^d - H_2^1}{d1v^c + H_2^1}} \tag{8}$$

$$V_I^c = \frac{d2v^c\, V_j^c - d3v^c\, V_{j+1}^c - (\boldsymbol{\tau}_{\mathbf{I}}^{\mathbf{c}} \cdot \mathbf{n}) \cdot \mathbf{t}}{d1v^c + H_2^1} \tag{9}$$

$$C_I^c = \frac{d2p^c\, C_j^c - d3p^c\, C_{j+1}^c + \dfrac{D^d}{D^c}(d2p^d\, C_{j-1}^d - d3p^d\, C_{j-2}^d)}{d1p^c + \dfrac{D^d}{D^c}\, k\, d1p^c} \tag{10}$$

$$\left(\frac{\partial C^c}{\partial n}\right)_I = \frac{k\, d1p^d(d2p^c\, C_j^c - d3p^c\, C_{j+1}^c) - d1p^c(d2p^d\, C_{j-1}^d - d3p^d\, C_{j-2}^d)}{k\, d1p^d + \dfrac{D^c}{D^d} d1p^c} \tag{11}$$

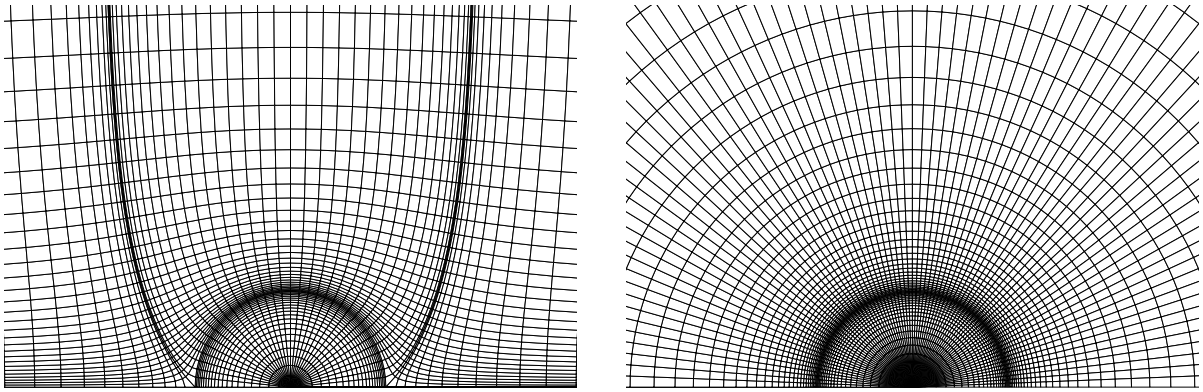


Figure 2: Left : LCE Mesh, Right : Polar Mesh

*2.5. Numerical procedure*

The set of conservation equations is solved using an inhouse code JADIM based on Finite Volume Method, developed in IMFT [26]. The algorithm of resolution relies on the projection method, where the diffusive-convective terms are evaluated first, then the pressure is resolved in order to satisfy the incompressibility condition. The numerical scheme of time advancement based on a second order Range-Kutta/Crank-Nichelson presents an efficient stability as explained in Rivero [26] Thesis. The viscous terms are calculated implicitly while the convective terms are evaluated explicitly. The spatial discretization is based on second order centred scheme. The pressure's resolution is performed independently inside

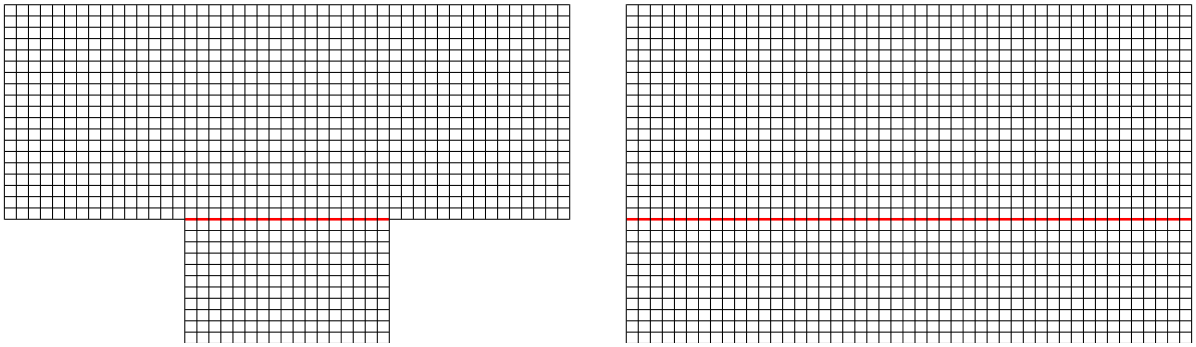


Figure 3: Left : Numerical domaine associated with the LCE Mesh, Right : Numerical domain associated with the Polar Mesh

and outside the droplet, using a Poisson solver.
The simulation strategy is performed as follows. First, hydrodynamics is solved at a given $Re$ number and viscosity ratio $\mu^*$ until a steady state is reached. The concentration equation is then solved in a frozen velocity field with an initial value of $C_0^d = 1$ and 0, respectively inside and outside the droplet, the calculation is then stopped as the mean solute dimensionless concentration inside the droplet goes below $10^{-5}$.

*2.6. Post-processing and notations*

Dimensionless parameters will be used in this study to analyse the results. Some of them were already seen in the dimensionless balance equations and the discretization of hydrodynamic and mass transfer quantities at the interface. Therefore results will be presented in terms of dimensionless ratios $\mu^*$, $\rho^*$ and $D^*$ which stands for dynamic viscosity ratio, density ratio and mass diffusivity ratio, respectively defined by :

$$\begin{cases} \mu^* = \dfrac{\mu^d}{\mu^c} \\ \rho^* = \dfrac{\rho^d}{\rho^c} \\ D^* = \dfrac{D^d}{D^c} \end{cases} \tag{12}$$

By convention, and for the sake of simplicity, the Reynolds and the Peclet numbers, will be based on the external physical properties and the droplet diameter :

$$\begin{aligned} Re &= \frac{U_0 \cdot d}{\nu^c} \\ Pe &= \frac{U_0 \cdot d}{D^c} \end{aligned} \tag{13}$$

The drag coefficient $C_D$ is calculated from the total drag force $F_D$ exerted by the uniform flow on the droplet using the classical definition :

$$C_D = 8\frac{F_{D,p} + F_{D,f}}{\pi \rho^c U_0^2 d^2} \tag{14}$$

The global Sherwood number is defined by the following expression (considering as driving force the difference between the instantaneous sphere average concentration and the free stream concentration):

$$Sh = \frac{1}{\overline{C^d}} \int_{drop} \left. \frac{\partial C^d}{\partial \mathbf{n}} \right|_I \cdot \sin(\theta) dS \tag{15}$$

Where $\overline{C^d}$ is the mean solute's concentration in the droplet, given by :

$$\overline{C^d} = 12 \int_0^R \int_0^\pi C^d(r,\theta) r^2 \sin(\theta) dr d\theta \tag{16}$$

The local Sherwood number is also considered defined by

$$Sh_\theta = -\frac{2}{\overline{C^d}} \left. \frac{\partial C^d}{\partial \mathbf{n}} \right|_I \tag{17}$$

At last, in the dimensionless framework considered here, the governing time-scale for the transport process is expressed by the Fourier number $Fo$ :

$$Fo = \frac{D^c t}{R^2} \tag{18}$$

## 3. Validations & discussions

### *3.1. Mesh sensibility*

The mesh sensitivity has been studied by refining either the radial and the angular mesh inside the droplet (see Figure 4), we recall that the cell size on the interface was chosen to fulfil the conditions discussed in Sec 2.4. In each case, the same expansion ratio is considered on each side of the interface in order to guarantee a smooth transition between the two liquid phases. Due to the structure of the external mesh (first type), an internal angular refining induces an angular refining in the outer region just above the droplet, and a radial refining is sometimes required outside the droplet to keep a good mesh quality. The sensibility of the drag coefficient $C_D$ Eq (14), and of the global Sherwood number Sh (Eq (15)) regarding the mesh size is reported in Tables 1 and 2 respectively.

Note that, for the sake of simplicity, only the asymptotic value of $Sh$ is reported in Table 2. No significant deviation is observed for the large range of conditions investigated (i.e. regardless of the viscosity ratio and/or the $Pe$ values) hence highlighting that mesh convergence is reached.

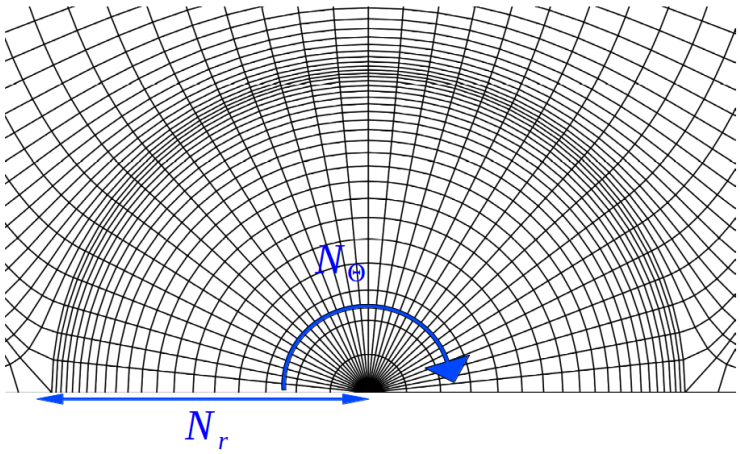



Figure 4: Radial and angular parameters of refining

| $\mu^*$ | Mesh $N_r \times N_\theta$ | | | |
|---|---|---|---|---|
| | $50 \times 80$ | $60 \times 100$ | $70 \times 100$ | $100 \times 120$ |
| 0.5 | 0.541 | 0.542 | 0.541 | 0.541 |
| 1 | 0.6598 | 0.6605 | 0.660 | 0.660 |
| 2 | 0.803 | 0.803 | 0.803 | 0.803 |

Table 1: Drag coefficient ($Re = 100$, $\rho^* = 1$)

| $Pe$ | Mesh $N_r \times N_\theta$ | | | |
|---|---|---|---|---|
| | $50 \times 80$ | $60 \times 100$ | $70 \times 100$ | $100 \times 120$ |
| 10 | 1.742 | 1.745 | 1.745 | 1.746 |
| 100 | 5.501 | 5.505 | 5.507 | 5.507 |
| 1000 | 12.404 | 12.413 | 12.399 | 12.385 |
| 10000 | 16.911 | 16.903 | 16.9 | 16.87 |

Table 2: Sherwood number ($Re = 100$, $\mu^* = 1$, $\rho^* = 1$, $D^* = 1$)

### *3.2. Validations*

#### *3.2.1. Drag coefficient*

The drag coefficient is a relevant criteria to validate hydrodynamic model. A good review of previous work can be found in [5]. Ranging from analytical solution of the drag coefficient

of the Hadamard-Rybczynski solution in creeping flow (Eq (19)), to various experimental correlations at intermediate and higher Reynolds numbers.

$$C_D(Re, \mu^*) = \frac{8}{Re}\left(\frac{2+3\mu^*}{1+\mu^*}\right) \tag{19}$$

For our purpose, we used the results reported by Feng and Michaelides [8] and by Oliver and Chung [21], the comparison is given in Table 3. Our results shows perfect agreement with these earlier works (deviation less then 1%), Figure 5.

| $\mu^*$ \Re | 1 | 10 | 20 | 50 | 100 | 150 | 200 |
|---|---|---|---|---|---|---|---|
| 0.05 | 17.98 | 2.45 | 1.45 | 0.7 | 0.39 | 0.28 | 0.23 |
| 0.2 | 19.14 | 2.72 | 1.6 | 0.79 | 0.45 | 0.32 | 0.25 |
| 0.333 | 19.96 | 2.87 | 1.7 | 0.85 | 0.49 | 0.35 | 0.28 |
| | [19.9] | [2.87] | [1.71] | [0.89] | | | |
| 0.5 | 20.78 | 3.03 | 1.81 | 0.92 | 0.54 | 0.39 | 0.31 |
| | (20.74) | (3.030) | (1.818) | (0.939) | (0.552) | | (0.317) |
| 1 | 22.43 | 3.34 | 2.04 | 1.08 | 0.66 | 0.49 | 0.39 |
| | (22.42) | (3.339) | (2.037) | (1.097) | (0.666) | | (0.397) |
| 2 | 24.09 | 3.66 | 2.26 | 1.25 | 0.8 | 0.61 | 0.5 |
| | (24.02) | (3.655) | (2.26) | (1.25) | (0.803) | | (0.504) |
| 5 | 25.76 | 3.99 | 2.49 | 1.42 | 0.95 | 0.76 | 0.64 |
| | (25.67) | (3.974) | (2.484) | (1.412) | (0.955) | | (0.646) |
| 10 | 26.51 | 4.14 | 2.6 | 1.49 | 1.02 | 0.82 | 0.71 |
| | (26.43) | (4.117) | (2.584) | (1.479) | (1.011) | | (0.716) |
| 15 | 26.8 | 4.19 | 2.63 | 1.52 | 1.04 | 0.84 | 0.73 |
| 100 | 27.33 | 4.29 | 2.71 | 1.57 | 1.08 | 0.88 | 0.76 |

Table 3: Drag coefficients ($\rho^* = 1$), Values in parentheses (Feng & Michalides [8]), Values in brackets (Oliver & Chung [21])

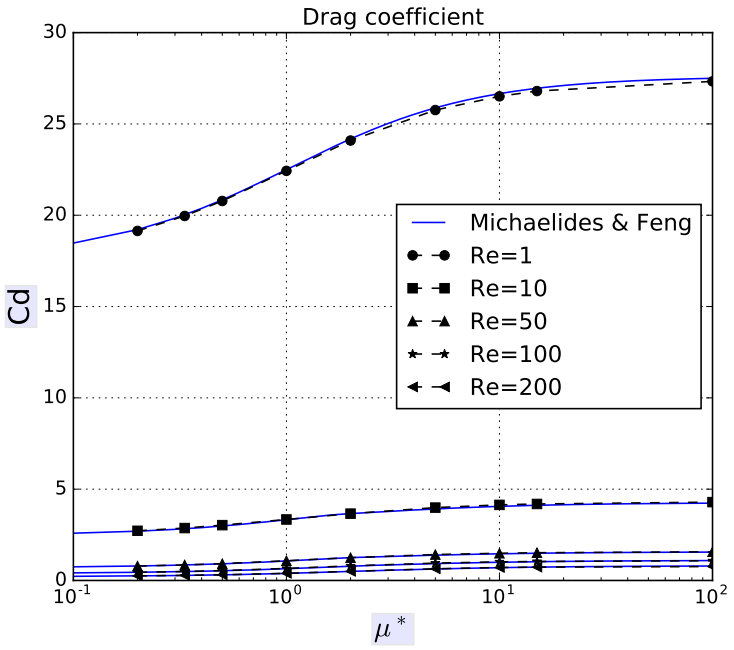



Figure 5: Drag coefficient in terms of viscosity ratios

*3.2.2. 1D diffusion : contact*

In order to test the validity of the implemented jump condition for the concentration, especially in the case of discontinuous concentration at the interface ($k$ different from 1), we considered the diffusion between two quiescent phases maintained in a perfect contact (see Figure 6 [right]). Both phases are supposed to be infinite in the directions $(x, z)$, so that the problem is 1D. Under the semi-infinite wall assumption, we can derive the analytical solution in Eq (20). For the numerical simulations, the following values were considered: $(D_1 = D_2; C_1^0 = 1; C_0^0 = 1)$, and studied the influence of the Henry coefficient, responsible for the discontinuity of the concentration at the interface. The case is sketched in Figure 6(right) with the boundary conditions used. The simulation results are in excellent agreement with the analytical solution ( Figure 7), as the Fourier number becomes significant compared to 1, the infinite-wall is no longer valid. It can be noticed that the concentration discontinuity at the interface is well predicted by the simulation, and that the value of the concentration at the interface is independent of the time.

$$\begin{aligned} C_1^+ &= \left(\frac{D_2}{D_2 + k \cdot D_1}\right)\left(\frac{k \cdot C_2^0 - C_1^0}{C_2^0 - C_1^0}\right) erfc(-u_1) \\ C_2^+ &= \left(\frac{D_1}{D_2 + k \cdot D_1}\right)\left(\frac{k \cdot C_2^0 - C_1^0}{C_2^0 - C_1^0}\right) erfc(u_2) \end{aligned} \tag{20}$$

$$\begin{cases} C_1^+ = \dfrac{C_1 - C_1^0}{C_2^0 - C_1^0} \\ C_2^+ = \dfrac{C_2 - C_2^0}{C_1^0 - C_2^0} \\ u_1 = \dfrac{y}{2\sqrt{D_1 t}} \quad for \quad y < 0 \\ u_2 = \dfrac{y}{2\sqrt{D_2 t}} \quad for \quad y > 0 \end{cases} \tag{21}$$

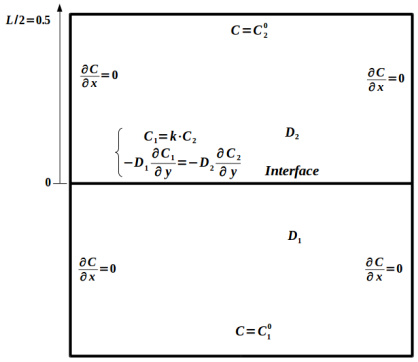



Figure 6: Left : Temperature distribution, Right : Boundary conditions

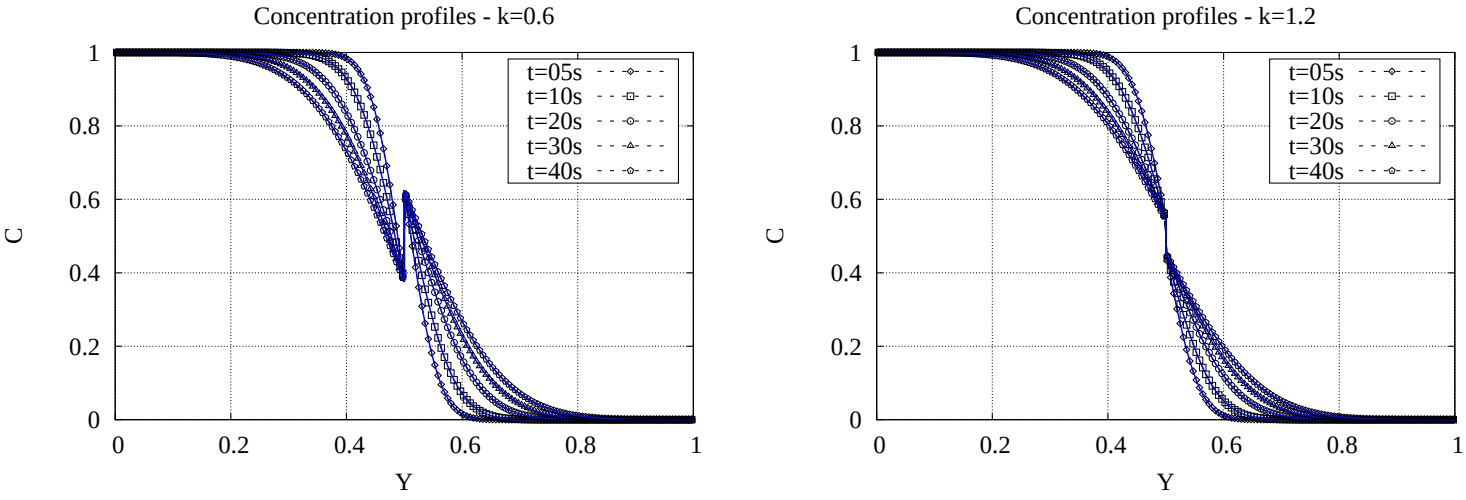



Figure 7: Time evolution of the concentration profile along the vertical line (Simulation : symbols, Analytical solution : blue line)

*3.2.3. 1D diffusion : Sphere*

The basic problem of heat or mass transfer inside a droplet is that of the pure diffusion problem ($Pe = 0$ and $Re = 0$), The instantaneous radial profile of the normalized concentration $C^d$ is given by Newman [20] equation.

$$C^d = 1 + \frac{2}{r}\sum_{n=1}^{+\infty} \frac{(-1)^n}{n\pi} \exp\left(-(n\pi)^2 Fo^d\right) \sin\left(n\pi r\right) \tag{22}$$

Where $Fo^d = \dfrac{D^d t}{R^2}$ is the Fourier number related to the droplet. The instantaneous Sherwood number may be derived from the previous expression as

$$Sh = \frac{2\pi^2}{3} \frac{\sum_{n=1}^{+\infty} \exp\left(-(n\pi)^2 Fo^d\right)}{\sum_{n=1}^{+\infty} \dfrac{1}{n^2} \exp\left(-(n\pi)^2 Fo^d\right)} \tag{23}$$

The Sherwood number reaches the limiting value $Sh_{Newman} = 2\pi^2/3 \approx 6.58$ in the limit of $Fo \longrightarrow \infty$. Radial concentration profiles obtained by Eq (23) and by our DNS simulation are compared in Figure 8 for different dimensionless times. A perfect agreement can be observed between our simulations (symbols) and the Newman's solution (lines). The corresponding asymptotic Sherwood number estimated from our simulations is $Sh_\infty = 6.56$, which differs only by 0.2% from the Newman's results

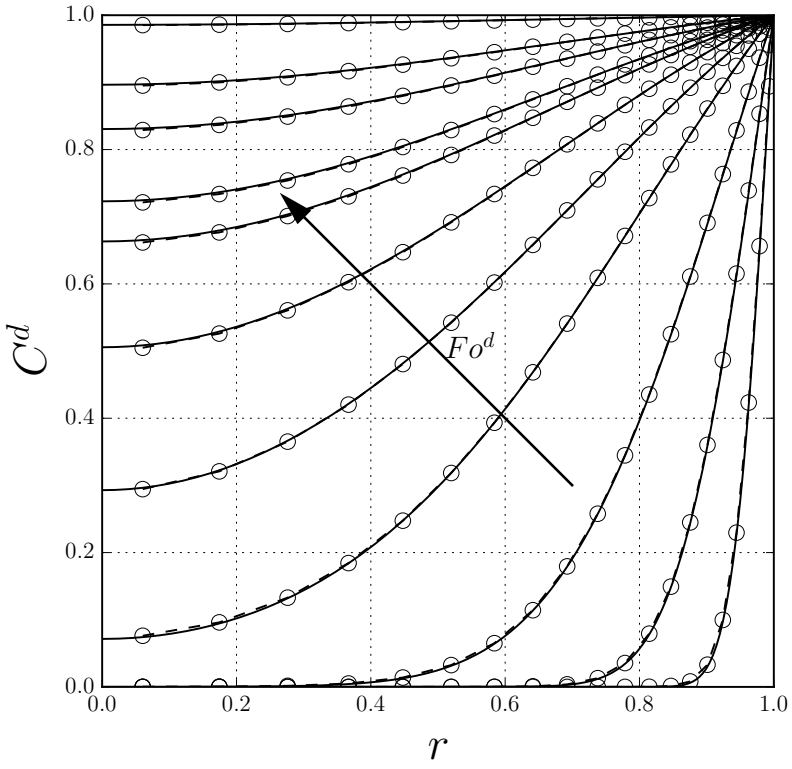



Figure 8: Temporal evolution of the concentration along the radius

*3.2.4. Internal problem : low Reynolds number*

We consider the transfer in the limit of a low Reynolds number. In such case, an analytical solution for the external and the internal flow is given by Hadamard-Rybczynski, in our

simulation the Reynolds number used is $Re = 0.1$. In the case of internal problem, the concentration is imposed by the continuous phase. We compare our results with available solutions from the literature. The simulations reported in Fig 9 are performed at viscosity ratio $\mu^* = 1$. The temporal evolution of the Sherwood number shows good agreement with Clift et al. [5]. It is worth noticing that as $\frac{Pe}{\mu^*+1} \longrightarrow 0$ the Sherwood number converges to the steady value given by Eq (23). While When $\frac{Pe}{\mu^*+1} \longrightarrow \infty$, an analytical solution of the Sherwood number is given by Kronig and Brink [16] in Eq (24). The Sherwood number corresponding to $Pe = 10^5$ is mingled with the one associated with Kronig and Brink Solution.

$$Sh = \frac{32}{3} \frac{\sum_{n=1}^{+\infty} A_n^2 \lambda_n \exp\left(-16\lambda_n Fo^d\right)}{\sum_{n=1}^{+\infty} A_n^2 \exp\left((-16\lambda_n Fo^d\right)} \tag{24}$$

Where $A_n$ and $\lambda_n$ are defined by the lists (25)

$$\begin{aligned} A_n &= [1.33 \quad 0.60 \quad 0.36 \quad 0.35 \quad 0.28 \quad 0.22 \quad 0.16] \\ \lambda_n &= [1.678 \quad 8.48 \quad 21.10 \quad 38.5 \quad 63.0 \quad 89.8 \quad 123.8] \end{aligned} \tag{25}$$

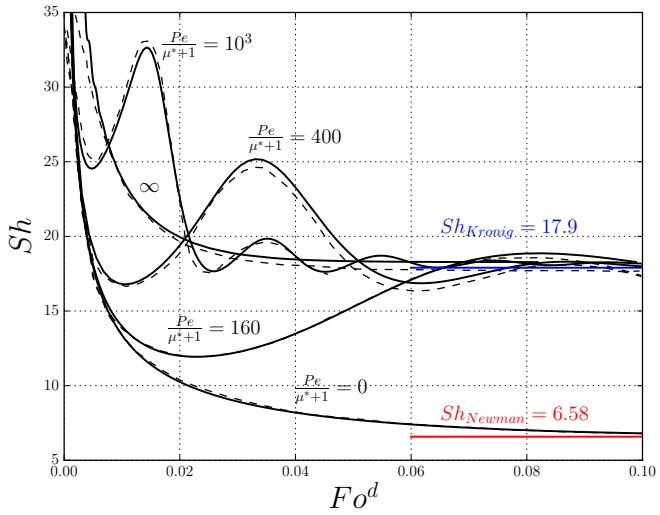



Figure 9: Temporal evolution of the Sherwood number for different values of $Pe/(\mu^*+1)$, solid line : present results, dashed lines [5]

Juncu [14] work has been adopted to investigated the evolution of the local Sherwood profile (Figure 10). The temporal evolution of $Sh_\theta$ along the interface shows excellent agreement with Juncu's results.

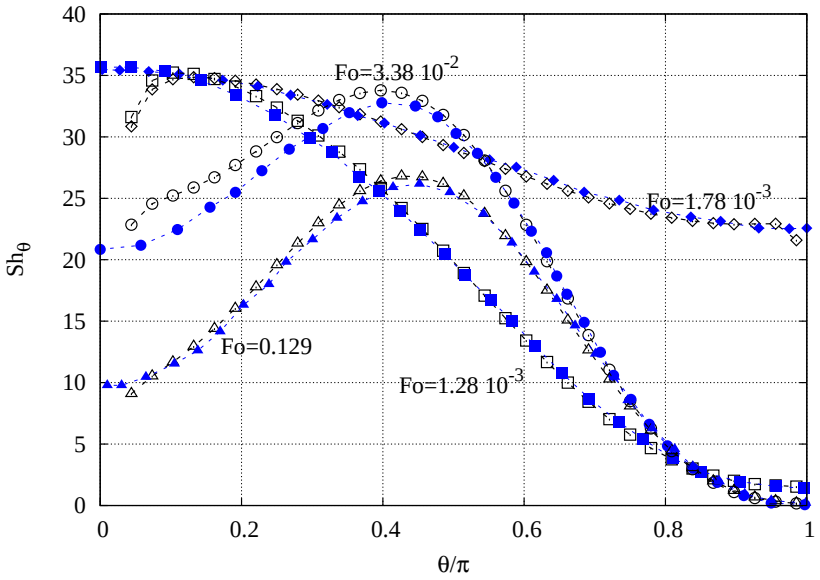



Figure 10: Local Sherwood number profiles for different Fourier Number, - blue : Juncu's results [14], - black : present calculation ($Pe = 1000$, $\rho^* = 1$, $\mu^* = 1$, $D^* = 1$ )

*3.2.5. Conjugate problem : low Reynolds number*

In the case of comparable mass resistance in both phases, one must resolve the concentration equation in both the internal and the external phase with jump conditions at the interface. We consider a droplet in a small Reynolds flow (i.e. $Re = 0.1$), the viscosity ratio considered in this study is set to be one $\mu^* = 1$. As the Peclet number increases the effect of convection becomes increasingly significant, hence the internal recirculation's effect on the Sherwood number evolution. Figure 11 (top left) depicts a temporal evolution of the Sherwood number. A comparison with Oliver and Chung [23] works shows good agreement. For the studied Peclet number range, the Sherwood number temporal settles to a steady value $Sh_{st}$, Table 4 reports the latter values which are consistent with previous works.

| $Pe$ | 50 | 100 | 200 | 500 | 1000 |
|---|---|---|---|---|---|
| Present calculation | 2.72 | 3.6 | 4.8 | 7.19 | 9.14 |
| Olivier & Chung | 2.67 | 3.6 | 4.8 | 7.2 | 9.2 |

Table 4: Steady Sherwood number $Sh_\infty$ for $Re = 0.1$ and $\mu^* = 1$

A parametric study has been conducted, always on the limit of the Reynolds number. three key parameters have been studied, the mass diffusivity ratio, the Henry coefficient and the viscosity ratio. The impact of these coefficients seems to be significant on the Sherwood

number. Kleinman and Reed [15] results have been token as a reference to validate our simulations, Figure 11 summarizes the main results of the parametric study. An increase in the distribution coefficient $k$, Which means a decrease in the solubility of the solute in the continuous phase, leads clearly to a decrease in the mass transfer rate. It is worth to note that oscillations are damped as the Henry coefficient increases (the effect of internal recirculation is hence linked to Henry coefficient as well). In Figure 11 the temporal evolution of $Sh$ has been displayed for a Peclet number of $Pe = 1000$ and different values of the diffusivity ratio $D^*$, it can be noticed that the frequency of the internal oscillations in $Sh$ is independent of the diffusivity ratio. This confirms the explanation that these oscillations are due only to the internal recirculation and not the diffusion. $D^*$ is a key parameter allowing to shift the mass resistance into either the internal or external phase. Theoretically, the Sherwood number evolution must converges to the profiles associated to the internal problem. For $D^* = 0.25$ the Sherwood temporal evolution converges toward the value $Sh = 15.327$ which is lower than 17.9, for $D^* = 0.1$ it has been found that the Sherwood number asymptotically value converges toward $Sh = 17.07$ which represents 95% of the limiting value.

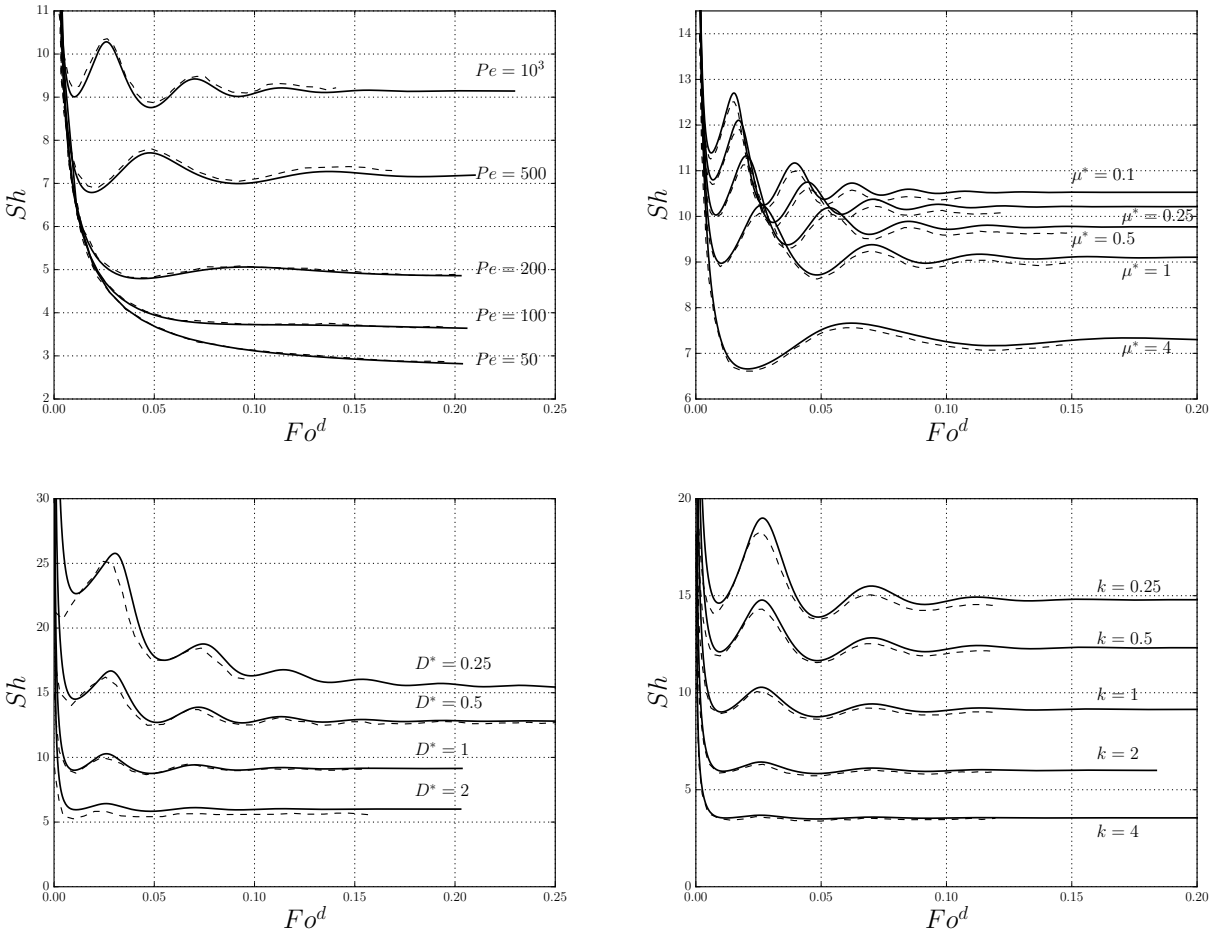



Figure 11: Temporal evolution of Sherwood number [$Re = 0.1$, $Pe = 1000$] (solid lines represent present results, dashed lines Kleinman & Reed [15] (bottom and top right), Oliver & Chung [23](top left) )

The evolution of the solute concentration depends significantly on the problem parameters. The effect of the Peclet number of temporal evolution of the solute concentration distribution has been highlighted if Figure 12 for diffusive process (i.e. $Pe = 10$), the diffusion of the solute is almost symmetric. For $Pe = 1000$ (convective process) Figure 13, one can observe the effect of the internal recirculation on the solute distribution, after a certain time the process became diffusive limited from a torus located in the vortex zone toward the interface, this state represents the steady regime observed in the Sherwood temporal evolution.

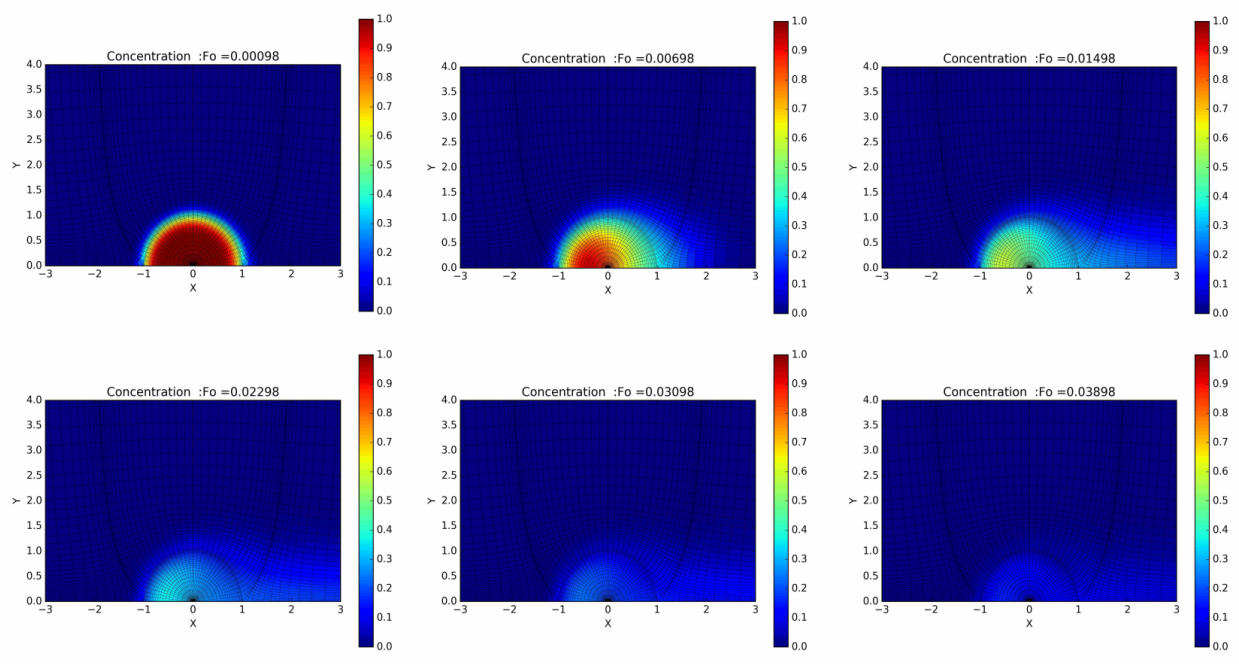



Figure 12: Temporal evolution of concentration distribution ($Re = 10$, $\mu^* = 1$, $D^* = 1$, $Pe = 10$)

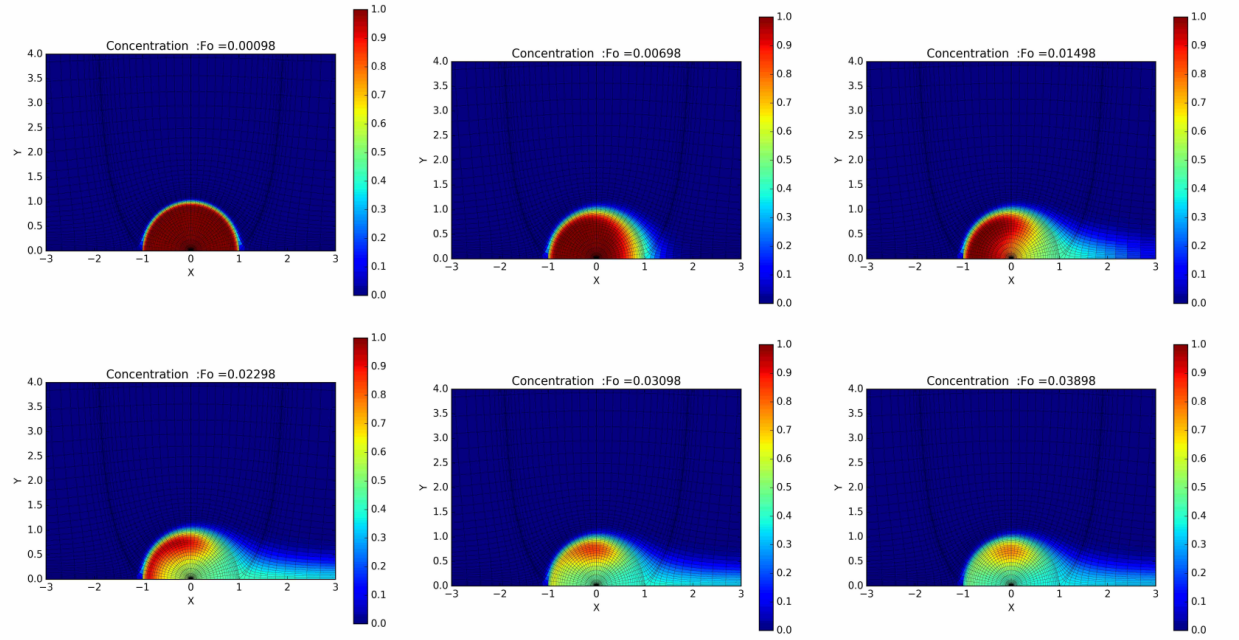



Figure 13: Temporal evolution of concentration distribution ($Re = 10$, $\mu^* = 1$, $D^* = 1$, $Pe = 1000$)

## 4. Results & discussion

### *4.1. Hydrodynamics*

#### *4.1.1. Drag coefficient*

In creeping flow, (e.g. small $Re$), the drag coefficient of Particle/Bubble for creeping flow is given by : $C_d^{bubble}(Re) = 16/Re$ and $C_d^{particle}(Re) = 24/Re$. Hence for small $Re$ Equation (19) can be written as :

$$C_D(Re, \mu^*) = \frac{C_D^{bubble} + \mu^* C_D^{particle}}{1 + \mu^*} \tag{26}$$

In order to verify the validity of equation 26 in the studied range of $Re$ and $\mu^*$. It is interesting to start by noticing that all the curves of the droplet drag coefficient $C_D(Re, \mu^*)$ (Figure 14) lie between the Mei & Klausner correlation for bubble [19] and Shiller & Neuman one for rigid particle [5] (i.e. $C_D^{bubble}(Re) \leq C_D(Re, \mu^*) \leq C_D^{Particle}(Re)$)

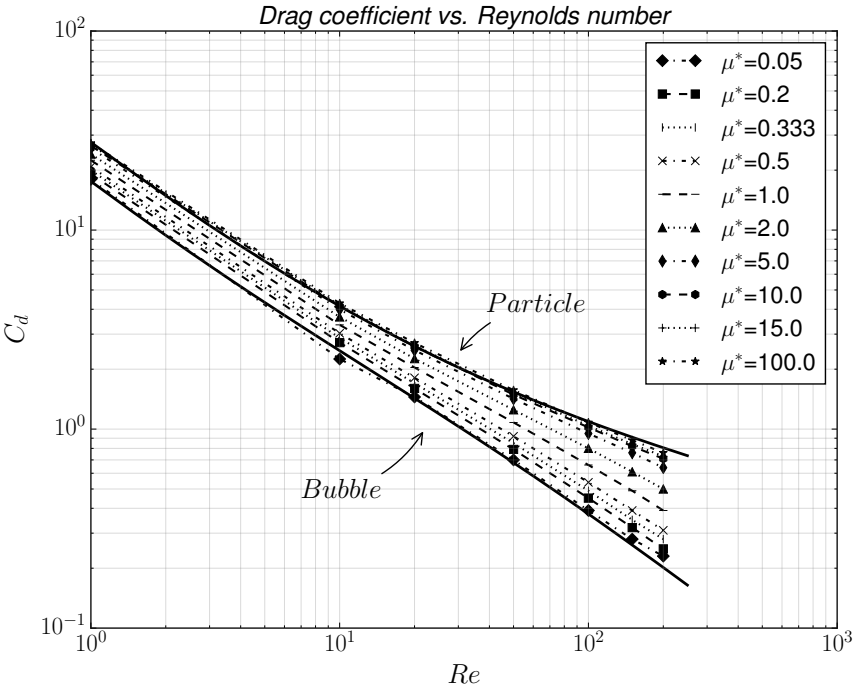



Figure 14: Drag coefficients, makers : present calculation, continuous line : correlations [19], [5]

Table 5 and Figure 15 compare the present results of drag coefficient with values using the simple correlation in Eq (26). Interestingly Equation (26) yields a very good approximation of the real values calculated by simulation. The viscosity ratio takes different values

which explains several symbols for the same Reynolds number in Figure 15.

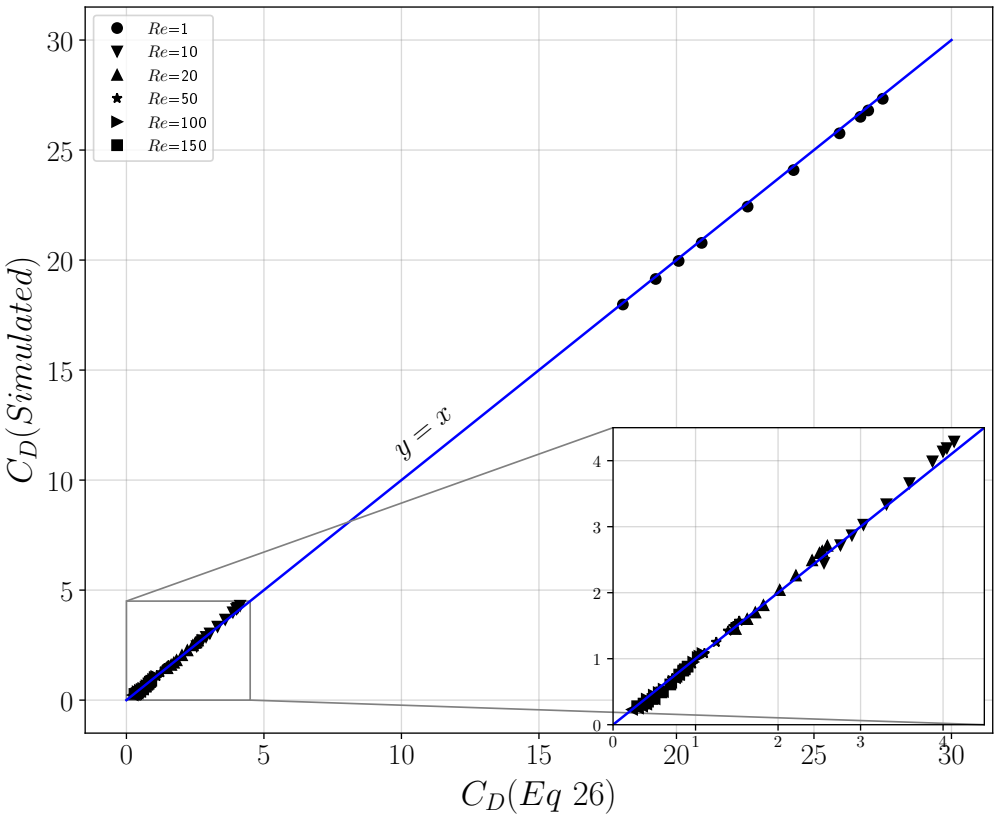



Figure 15: Parity plot of the drag coefficient: symbols : present simulations vs Eq (26), blue lines : $y = x$ (Each Reynolds number contains different viscosity ratios)

| $\mu^* \backslash Re$ | 1 | 10 | 20 | 50 | 100 | 150 | 200 |
|---|---|---|---|---|---|---|---|
| 0.5 | 20.78 | 3.03 | 1.81 | 0.92 | 0.54 | 0.39 | 0.31 |
| | (20.916) | (3.035) | (1.822) | (0.964) | (0.613) | (0.477) | (0.403) |
| 1.0 | 22.43 | 3.34 | 2.04 | 1.08 | 0.66 | 0.49 | 0.39 |
| | (22.587) | (3.314) | (2.019) | (1.1077) | (0.733) | (0.585) | (0.503) |
| 2.0 | 24.09 | 3.66 | 2.26 | 1.25 | 0.8 | 0.61 | 0.5 |
| | (24.258) | (3.593) | (2.216) | (1.251) | (0.852) | (0.693) | (0.604) |
| 5.0 | 25.76 | 3.99 | 2.49 | 1.42 | 0.95 | 0.76 | 0.64 |
| | (25.929) | (3.872) | (2.412) | (1.394) | (0.972) | (0.802) | (0.704) |

Table 5: Comparison between present calculation of drag coefficient and Eq (26) between parentheses

The dependence of $C_D$ on the density ratio has been proven insignificant by Feng and Michaelides [8]. This result is supported by our present work (Table 6).

| Re / $\rho^*$ | 0.1 | 0.5 | 1 | 5 | 10 |
|---|---|---|---|---|---|
| 10 | 3.345 | 3.345 | 3.344 | 3.342 | 3.342 |
| 50 | 1.088 | 1.086 | 1.083 | 1.07 | 1.07 |
| 100 | 0.671 | 0.667 | 0.662 | 0.66 | 0.66 |

Table 6: Drag coefficient (density ratio effect)

*4.1.2. Separation angle*

For intermediate to high Reynolds flow and viscosity ratio, an external circulation may occur in the droplet's rear. Unlike the particle case, for a circulating drop, the internal circulation delays both the onset of flow separation and wake formation in the external fluid. The separation angle $\theta_d$ measures the angle at which the external boundary layer is detached from the sphere surface. This angle might characterize as well the position at which the vorticity at the interface (Eq (27)) changes sign. Clift et al. [5] show that in the solid particle case, the flow is unseparated for $0 < Re < 20$, then a steady wake region is then developed for $20 < Re130$. $Re = 20$ represents the onset of separation. The authors report a correlation of the separation angle (Eq (28)) which is valid for $20 < Re < 400$.

$$\omega_I = \frac{\partial V_2^c}{\partial \xi_1}\bigg|_I - \frac{\partial V_1^c}{\partial \xi_2}\bigg|_I + H_2^1 V_2^c|_I - H_1^2 V_1^c|_I \tag{27}$$

$$\theta_d = 42.5\,[\log(Re/20)]^{0.483} \tag{28}$$

For a gas bubble in liquid uncontaminated with surfactants, no separation is predicted ($\theta_d = 0$ even for Reynolds numbers as high as 200 [5], it has been supported by our results for small viscosity ratios. Figure 16 shows the vorticity (Eq (27)) profiles along the interface for different configurations. We note that for a given Reynolds number (here $Re = 100$), as we increase the viscosity ratio the difference between the extremums increases, if $\mu^* \geq 5$, vorticity changes sign, which proves that an external separation occurs at an angle where $\omega_I = 0$.

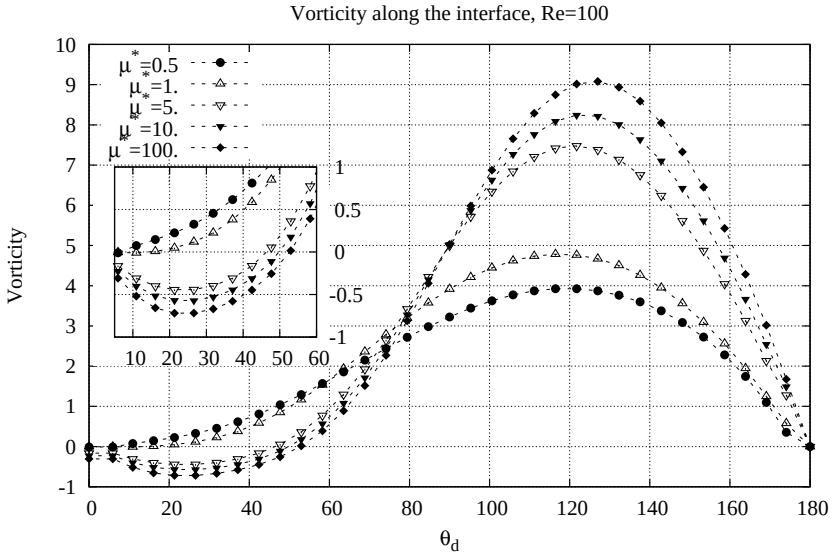



Figure 16: Vorticity profiles along the interface ($Re = 1$, $\rho^* = 1$)

Tables 7 and 8 report the angles of separation for different ($Re$,$\mu^*$) and some corresponding streamlines. Followinf the same reasoning as what it has been presented in the drag coefficient section, we adapt the previous correlation Equation (28) so that our results may be correlated in the studied range of ($Re$,$\mu^*$). As $\theta_d^{bubble} = 0$ for the considered Reynolds range, we multiply Eq (28) by $\mu^*/(1 + \mu^a st)$ (Eq (29)). Figure 17 shows the comparison between our results and the new correlation (e.g. Eq (29)). With an error bar of $\pm 1.5°$, the correlation yields satisfactory results.

$$\theta_d = 42.5\,[\log(Re/20)]^{0.483}\,\frac{\mu^*}{1+\mu^*} \tag{29}$$

| $\mu^*$ / $Re$ | 50 | 100 | 150 | 200 |
|---|---|---|---|---|
| 3 | no | 41 | 46 | 48 |
| 5 | 34 | 46 | 51 | 55 |
| 10 | 37 | 50 | 55 | 59 |
| 15 | 38 | 51 | 57 | 61 |
| 100 | 40 | 53 | 60 | 65 |

Table 7: Rounded separation angles

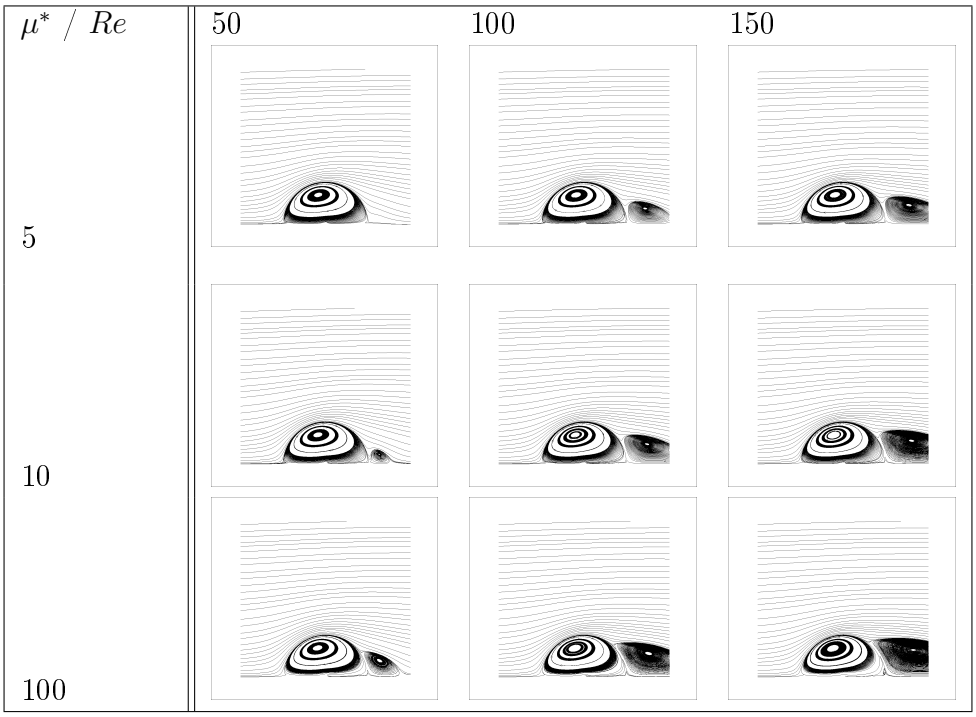



Table 8: Streamlines

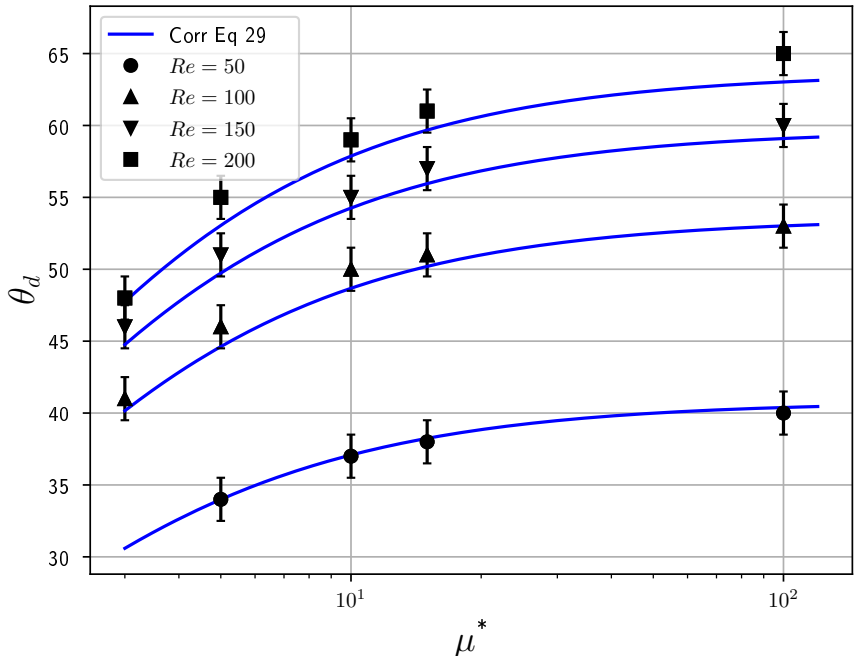



Figure 17: Separation angle : symbols : present simulations, blue lines : correlation Eq (29)

We can characterize the presence or the absence of the external recirculation by a schematic curve (Figure 18). In the pink region (i.e. below the curves) the external flow is unseparated, whereas an external recirculation will appear in blue area. As $\mu^*$ tends to high values, the droplet behaves such a particle which justify that the critical Reynolds number of separation is the onset of separation in the case of particle, hence $Re \longrightarrow 20$. However for low viscosities, the bubble-like behaviour is observed and no separation occurs.

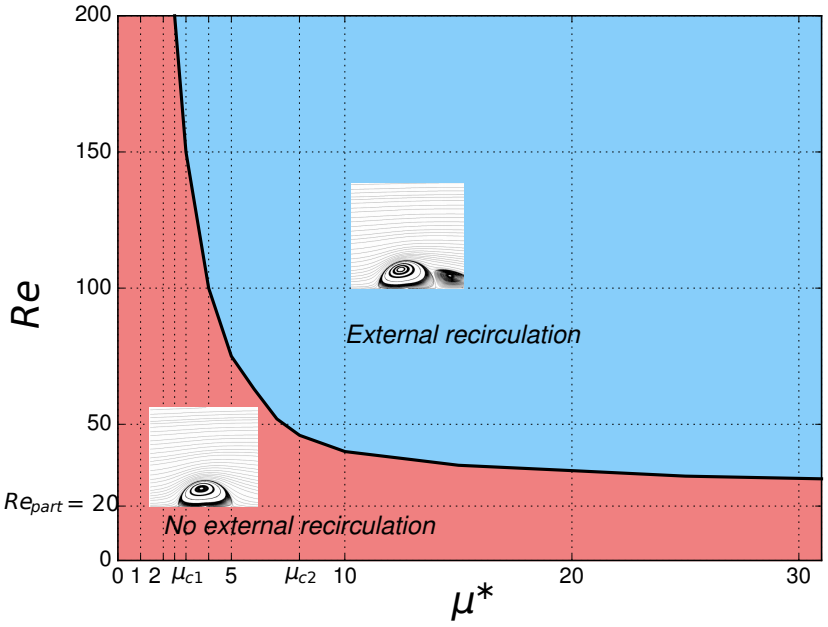



Figure 18: Schematic external bifurcation curve ( $\rho^* = 1$)

*4.2. Mass transfer*

*4.2.1. Local quantities*

In DNS calculations we can easily access more information about all relevant variables. In this section we focus on the behaviour of the concentration distribution along the interface and the corresponding local Sherwood number.

Logically, as the solute migrates from the droplet to the continuous phase, the droplet mean concentration decreases. The same trend is globally observed with the interface concentration. Interestingly a different evolution is evidenced regarding the ratio between the interface concentration and the droplet mean concentration. Indeed, steady evolution has been detected for the ratio in question Figures 19. The steady regime occurs at $Fo^d = 0.1$ regarding the studied configuration. The same trend was encountered with the local Sherwood number (i.e. Eq (17)). Figures 20 depicts the temporal evolution of the local Sherwood number profile, all curves converge toward a steady curve that depends only on $\theta$ and potentially problem parameters. For small times, $\overline{C^d} \approx 1$, the concentration gradient is generally important in the droplet front at the stagnation point, this justifies the profiles of $Sh_\theta$ for small times.

It is important to note that in some configurations, namely low $Pe$ or high $\mu^*$, the steady

behaviour is hardly reached before the droplet is "empty". In fact, in such configurations the drop mean concentration is critically low before global or local Sherwood number settle to steady trend.

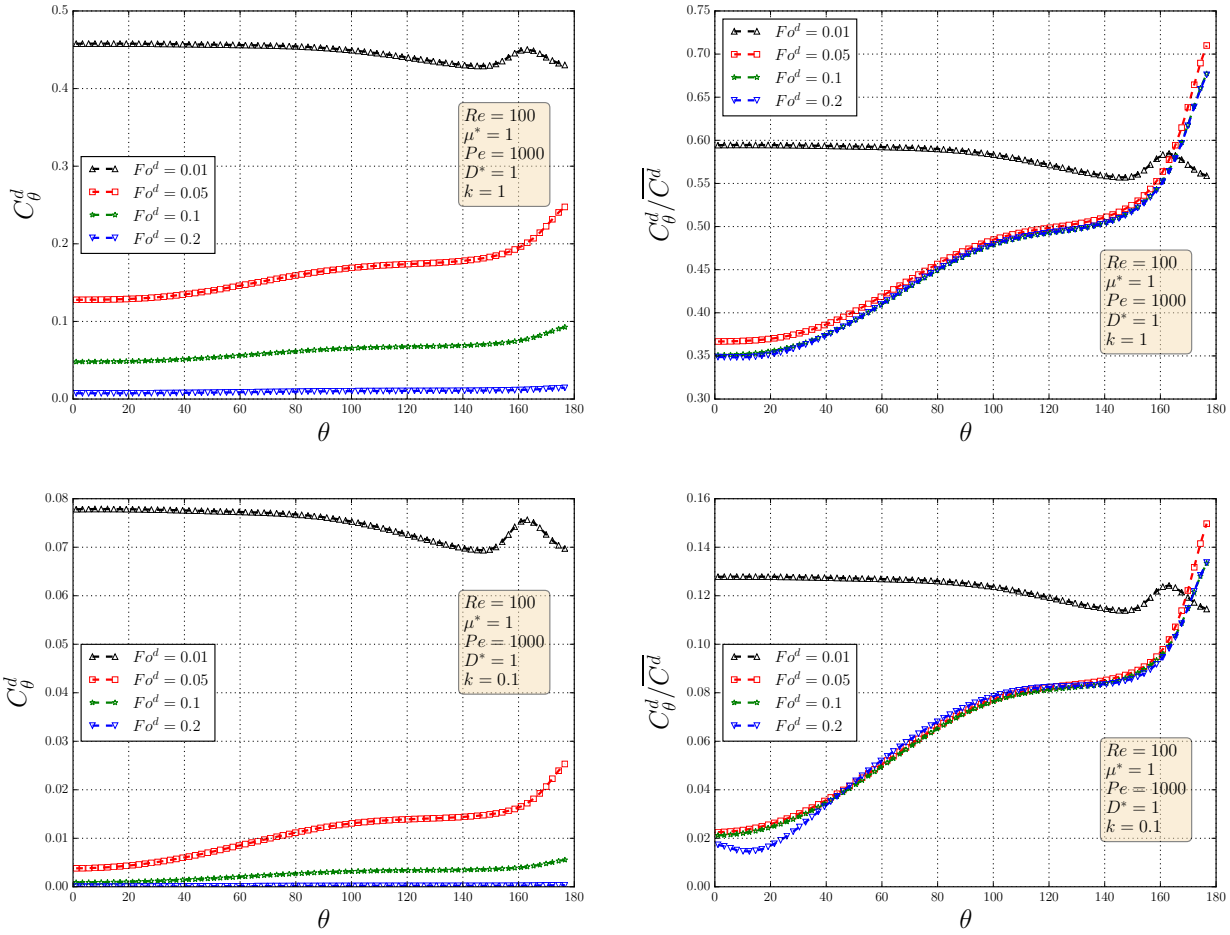



Figure 19: Left : Temporal evolution of interface concentration profile, Right : Temporal evolution of the ratio $C^d_\theta(\theta, Fo^d)/\overline{C^d}$

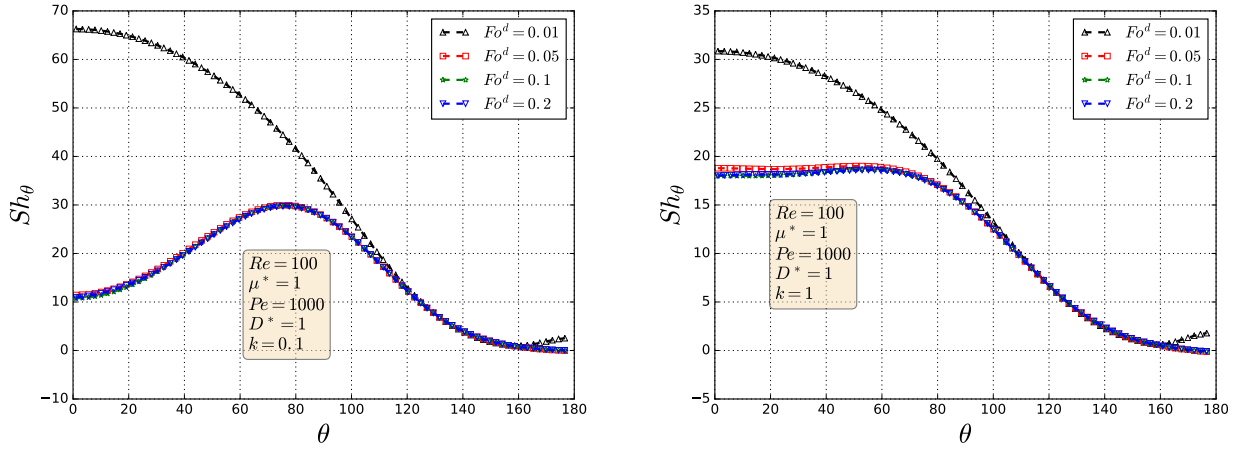



Figure 20: Temporal evolution of local Sherwood number

As it has been shown before, hydrodynamic parameters ($Re$, $\mu^*$) impacts significantly the vorticity along the interface. The same observation is valid of the interface velocity as shown in Figure 21. For a given $Re$ (Here $Re = 100$), as the viscosity ratio increases, the droplet behaviour approaches that of a rigid particle, and the interface velocity decreases. It's worth reminding that interface vorticity changes sign with the appearance of the external recirculation, which is the case at $\mu^* = 5$. For a given $Pe$, increasing $\mu^*$ hinders the interface motion which causes a decrease of the surface concentration gradient at the interface and the local Sherwood number. For the configuration $Re = 100$,$Pe = 1000$,$D^* = 1$, the steady state of the local Sherwood number is reached at around $Fo^d \approx 0.1$. Figure 22 compares the steady local Sherwood number for different $\mu^*$. In droplet's front, and for angles lower then 40°, the local Sherwood number increases with $\mu^*$ for both the $k = 0.1$ and $k = 1$ cases. The impact of viscosity ratio on the local Sherwood number is non trivial. For $\mu^* = 5$, due to the external recirculation, the solute is trapped in the vicinity of the recirculation, this latter feeds in return the droplet which results in a change of the concentration gradient sign at the droplet's rear, therefore, the local Sherwood number is negative.

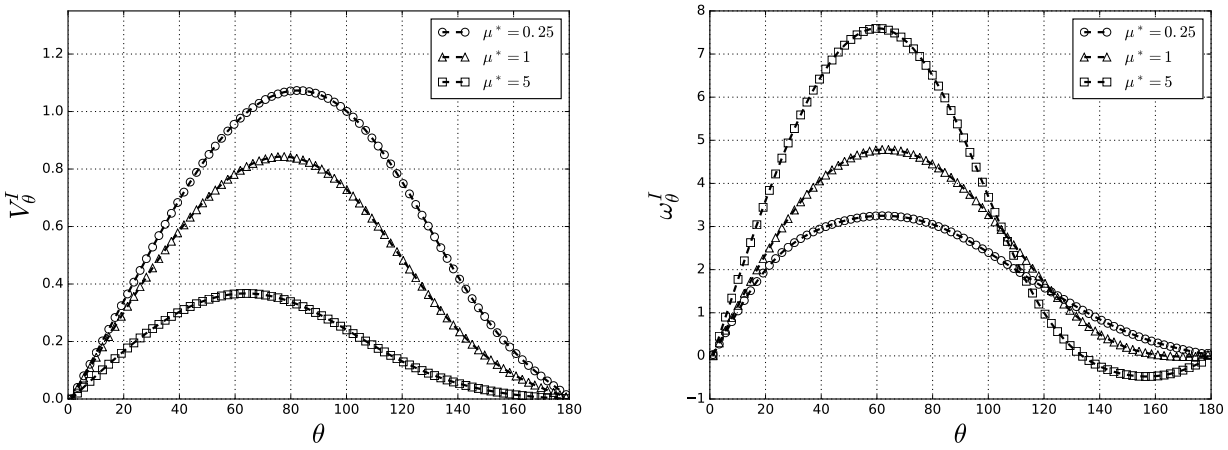



Figure 21: Left : Interface velocity, Right : interface vorticity

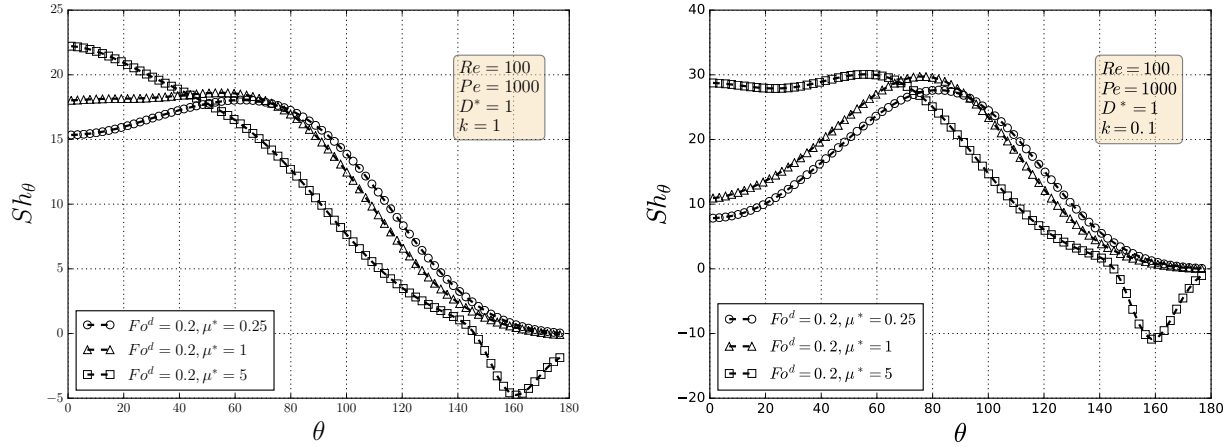



Figure 22: Asymptotic local Sherwood number : viscosity ratio impact

The effect of the Henry coefficient on the solution distribution is illustrated in Figure 23. All configurations were run with $Pe = 1000$, i.e. in convective transfer regime, which means that the effect of the internal circulation is enhanced. As the viscosity ratio increases, the circulation slows down and its center shifts toward the droplets front. The solute diffuses then slowly from the droplet to the continuous phase. For $k = 0.1$, the concentration at the interface is discontinuous which yields high concentration gradient and the transfer is increased.

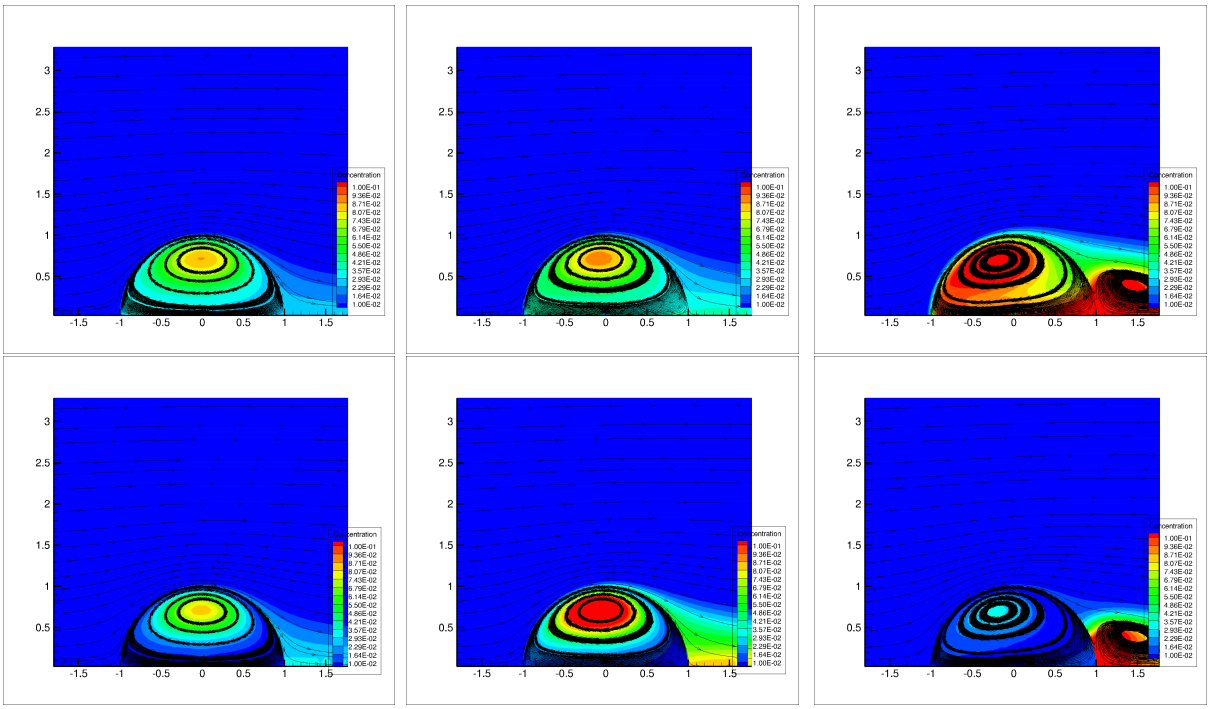


Figure 23: Concentration distribution and streamlines ($Fo^d = 0.15$, $Re = 100$, $Pe = 1000$, $D^* = 1$) - top : $k = 1$, bottom : $k = 0.1$ - From left to right : $\mu^* = 0.25, 1, 5$

### *4.2.2. Global Sherwood number*

In the limit of small $Re$, the existence of a steady state for the Sherwood number is non-trivial. It has been discussed by Johns and Beckmann [11], using the separation of variables, both the mass gradient at the interface and the bulk concentration decay exponentially, the ratio of the latter quantities (which defines the Sherwood number) converges toward a non zero value. Oliver and Chung [22], investigating numerically conjugate heat transfer from a translating fluid sphere for intermediate Reynolds up to 50, found the same asymptotic behaviour of the Sherwood number.

A parametric study has been conducted to investigate the effect of some key parameters on the $Sh$ for higher Reynolds numbers, Figures 24 show the evolution of global Sherwood number $Sh$ with time. The evolution of $Sh$ regarding problem parameters show similar trend as in creeping flow case (shown in Figure 11). An increasing viscosity ratio slows down the solute transfer and the $Sh$ converges slowly to an asymptotic value, it impacts significantly the transient regime, the oscillations magnitude and frequency. The same remark can be made regarding the $Re$ influence on the steady value of $Sh$ as shown in Figure 24. Mass transfer parameters, namely $k$ and $D^*$ still have big impact on the oscillations magnitude and the steady value of $Sh$.

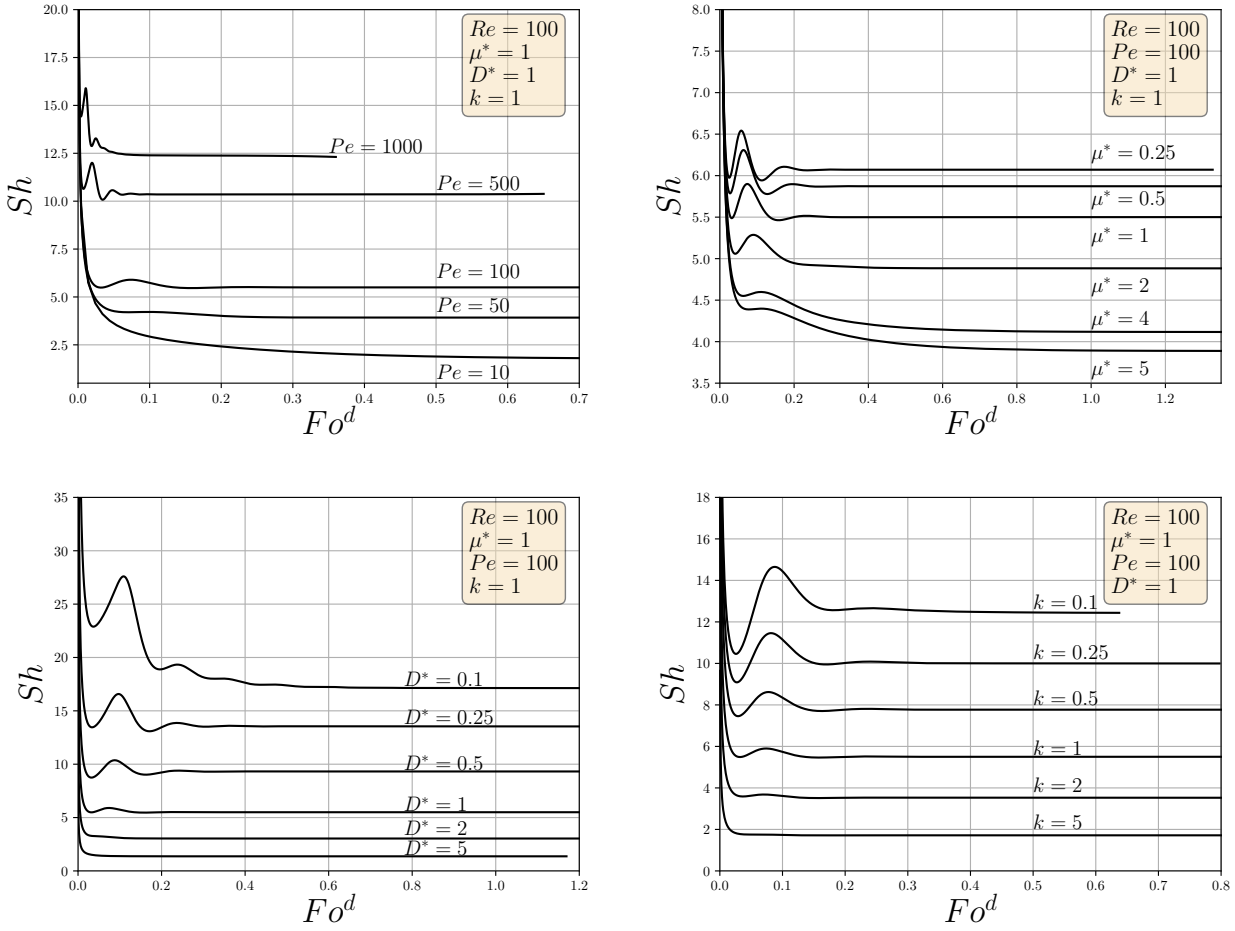



Figure 24: Temporal evolution of global Sherwood number - top left : $Pe$ impact, top right : $\mu^*$, bottom left : $k$ impact, bottom right : $D^*$ impact

It is worth reminding that for a given $Pe$, since it is the results of the product of $Re$ by $Sc$, different scenarios might occur. The impact of the hydrodynamics on the solute transfer is primarily governed by the Reynolds number. The effect of this latter depends strongly on $Pe$. For large $Pe$, an increasing $Re$ yiald drastic change in $Sh$ evolution as depicted in Figure 25 (right). However, for low $Pe$ corresponding to diffusive governed processes, $Re$ impacts barely the temporal evolution of the Sherwood number Figure 25 (left).

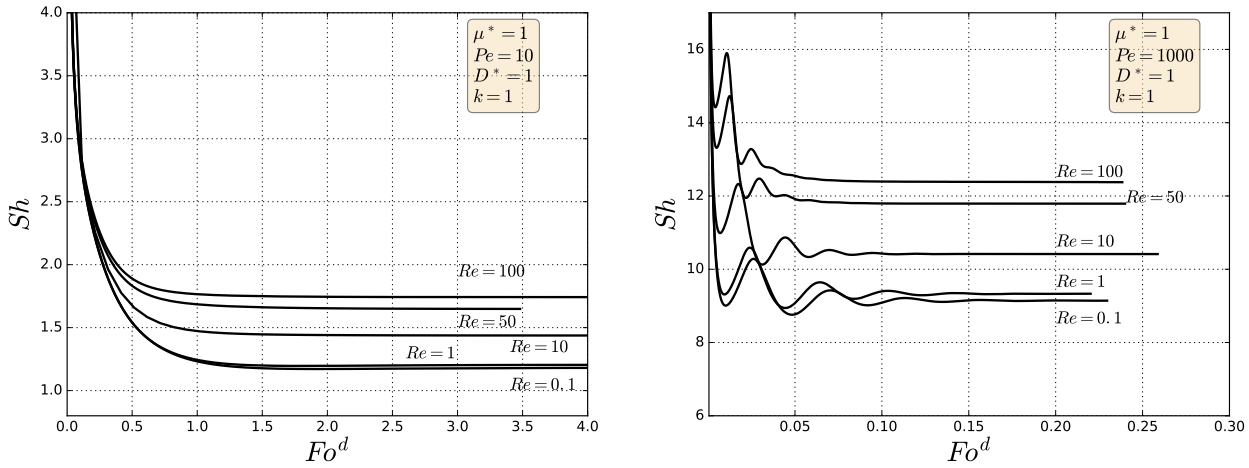



Figure 25: Temporal evolution of Sherwood number

The impact of the previous parameters on the mean solute concentration inside the droplet is furthermore depicted in Figure 26. The influence of the viscosity ratio in studied range is not significant as it is the case for the mass transfer parameters (Henry coefficient and diffusivity ratio). For a decreasing diffusivity ratio, the mass resistance is located in the droplet, therefore the solute mean concentration decays slowly from the droplet to the continuous phase (Figure 26 [bottom right]). It is interesting to note that for a variable $Pe$ (Figure 26 [top left]) and for small times, the transfer is mainly diffusive and the effect of the recirculation is not seen yet [5], therefore, the decreasing of $\overline{C^d}$ is independent of the Peclet number. The convective process triggers after $Fo^d \approx 10^{-3}$, subsequently the solute draining speeds up as $Pe$ increases.

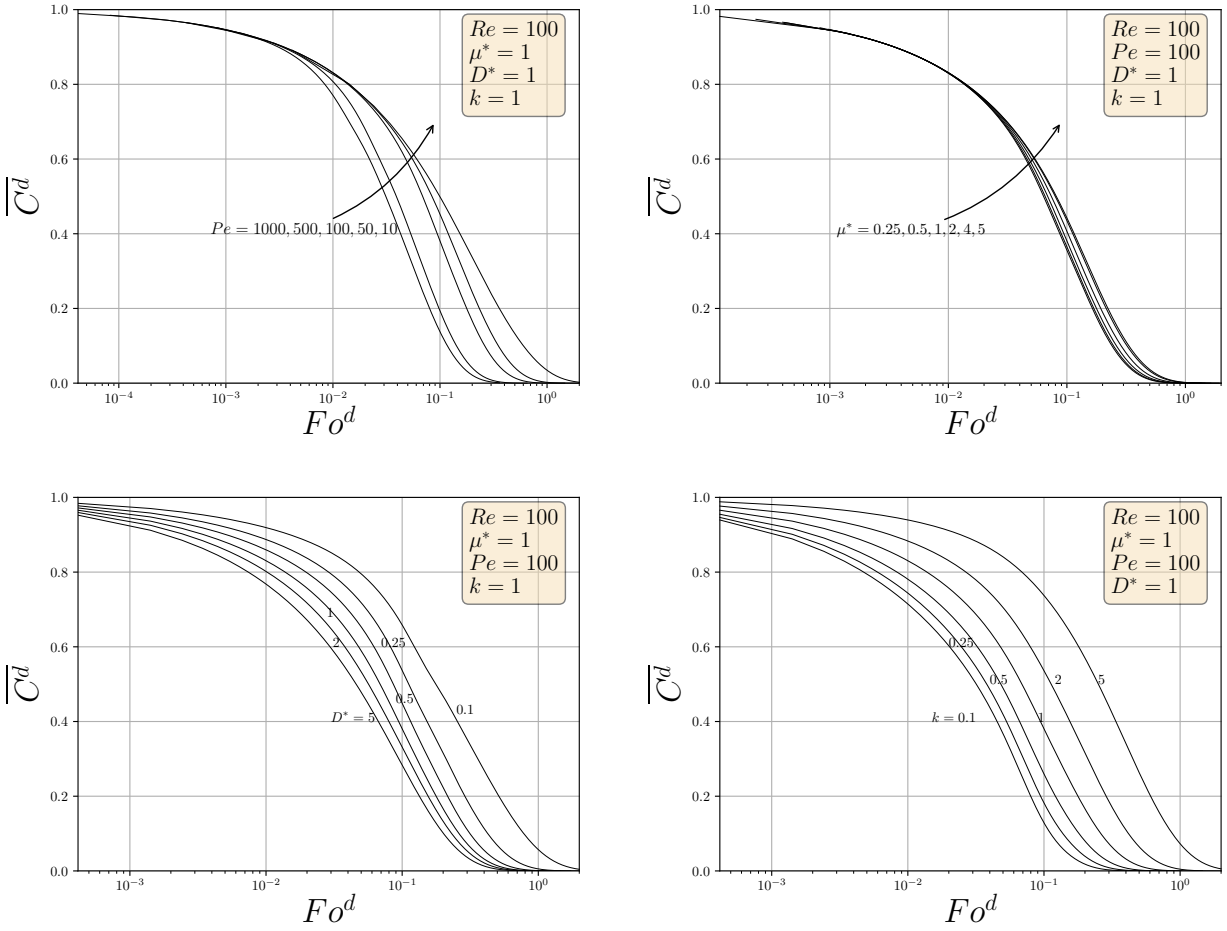



Figure 26: Temporal evolution of the mean concentration - top left : $Pe$ impact, top right : $\mu^*$, bottom left : $k$ impact, bottom right : $D^*$ impact

Throughout what has been previously presented, it has been found that for a given configuration, an increasing viscosity ratio $\mu^*$ is responsible for a slow transfer and a decreasing asymptotic value of the global Sherwood number (Figures 11 and 24). For a diffusive regime ($Pe = 100$), the previous rule is respected whether the Henry coefficient is small or equal to unity. However as the Peclet number increases, a curious behaviour occurs (Figure 27). For $k = 0.1$, as the viscosity ratio increases from 0.25 to 1, a slight increase of the steady value of the Sherwood number is obtained from 18.04 to 18.63. The present results has been proven independent of the used mesh. This behaviour is well illustrated in Figures 28. For Peclet numbers lower than 50, the Steady Sherwood number decreases monotonically with the viscosity ratio for the range of studied Henry coefficient $k$. However, for Peclet number equals to 1000, two behaviours are highlighted. On the one hand, for $k \geq 1$, $Sh_{asy}$ decreases monotonically with the viscosity ratio. On the other hand, as $k < 1$, $Sh_{as}(\mu^*)$ is no longer monotonic, an extremum occurs at $\mu^* < 2$ in the function $Sh_{as}(\mu^*)$ as is highlighted in Figure

28 . For small $Pe$ ($Pe < 10$), the slope of the decreasing function $Sh_{as}(\mu^*)$ decreases as the Henry coefficient increases, the asymptotic Sherwood number becomes then less dependent on the viscosity ratio. On the other hand, the steady Sherwood number keeps practically decreasing with slightly the same rate for $Pe = 1000$ and $k > 1$. A similar behaviour is illustrated when the diffusivity ratio varies for a given Henry coefficient ($k = 1$) in Figure **??**.

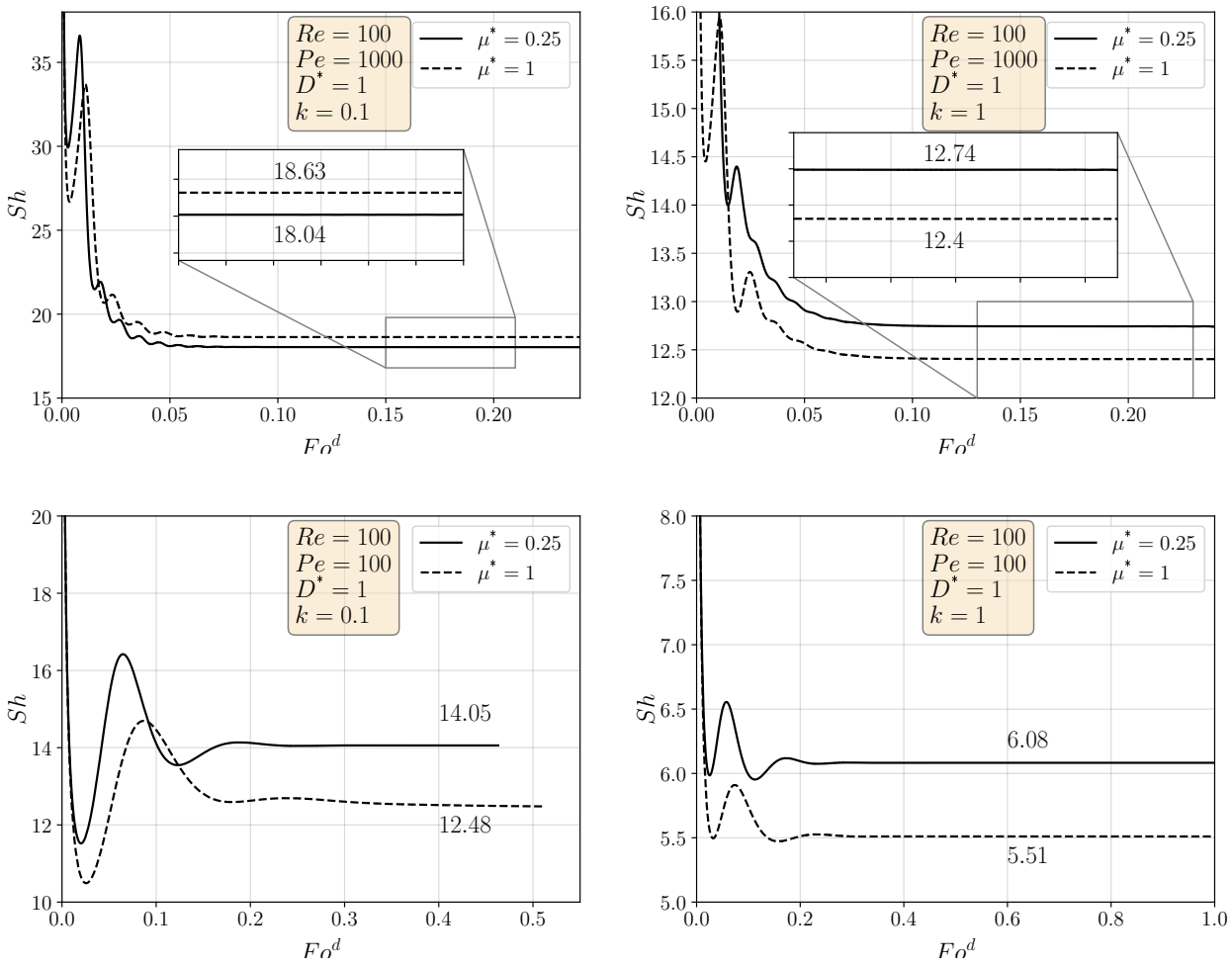



Figure 27: Temporal evolution of Sherwood number - Top : $Pe = 1000$, Bottom : $Pe = 100$

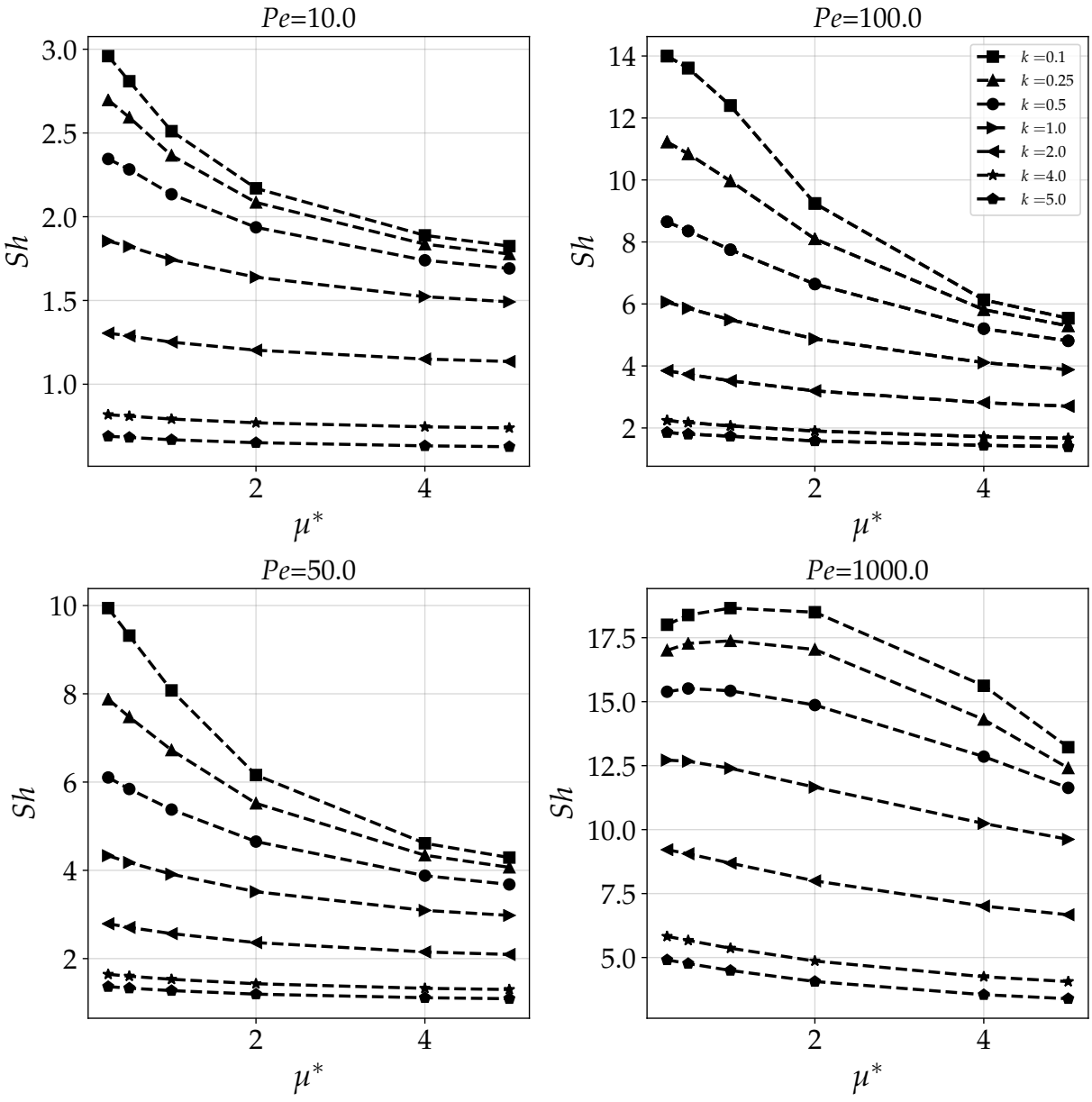



Figure 28: Asymptotic Sherwood number as function of the viscosity ratio for different Henry coefficient ($Re = 100$, $D^* = 1$)

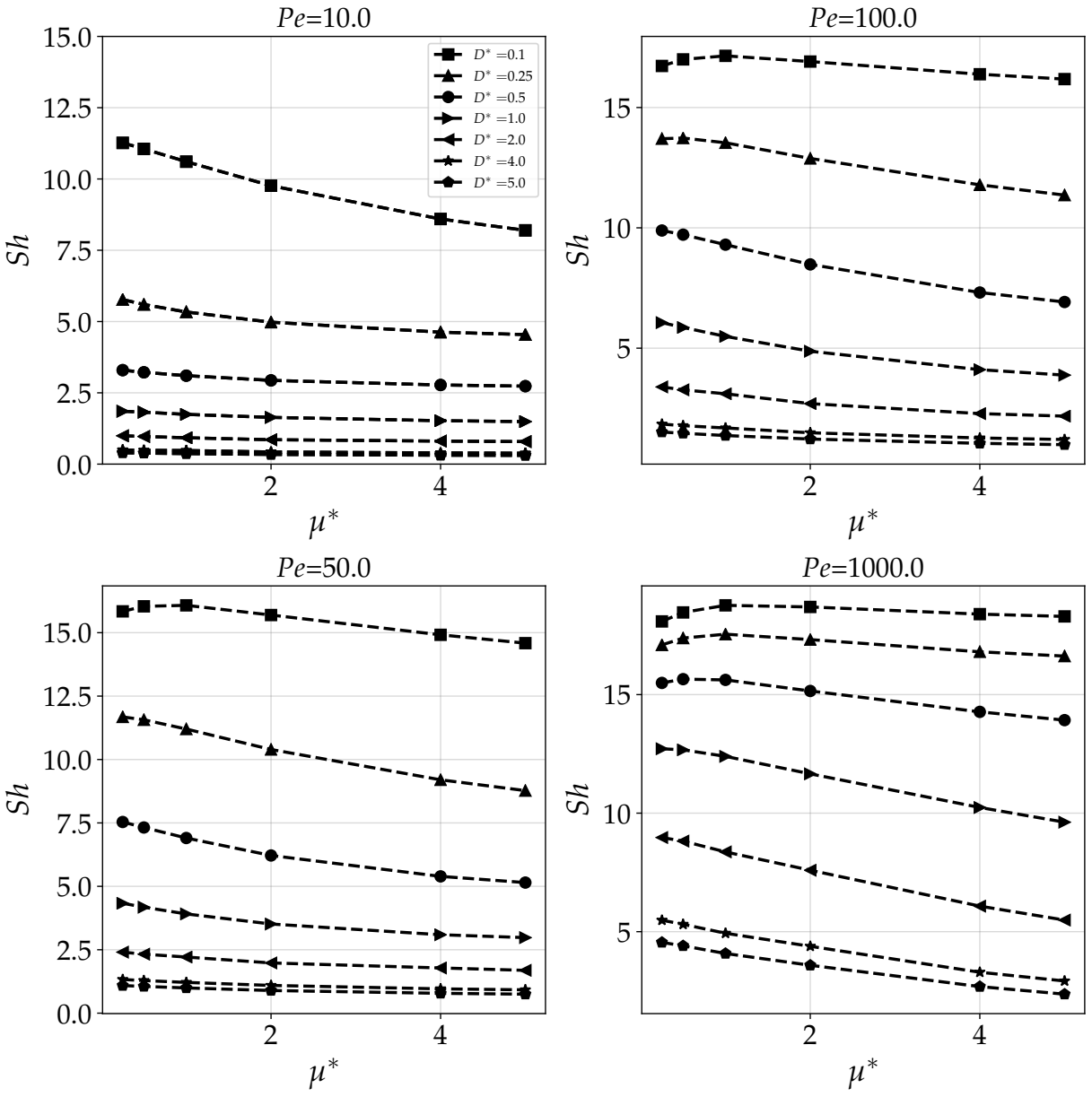



Figure 29: Asymptotic Sherwood number as function of the viscosity ratio for different diffusivity ratios ($Re = 100$, $k = 1$)

Table 9: Sherwood number

| | $k$ | $D^*$ | $\mu^* \backslash Pe$ | 10 | 50 | 100 | 500 | 1000 |
|---|---|---|---|---|---|---|---|---|
| $Re = 0.1$ | 1 | 0.5 | 0.25 | 2.352 | 5.239 | 7.183 | 12.005 | 13.5947 |
| | 1 | 0.5 | 1 | 2.1818 | 4.588 | 6.21 | 10.9848 | 12.736 |
| | 1 | 0.5 | 4 | 2.007 | 3.953 | 4.958 | 9.149 | 11.115 |
| | 1 | 1 | 0.25 | 1.288 | 3.007 | 4.137 | 8.237 | 10.213 |
| | 1 | 1 | 1 | 1.175 | 2.711 | 3.593 | 7.161 | 9.1 |
| | 1 | 1 | 4 | 1.063 | 2.454 | 3.077 | 5.576 | 7.2917 |
| | 1 | 2 | 0.25 | 0.641 | 1.7118 | 2.322 | 4.893 | 6.544 |
| | 1 | 2 | 1 | 0.573 | 1.546 | 2.062 | 4.129 | 5.577 |
| | 1 | 2 | 4 | 0.52 | 1.383 | 1.815 | 3.2 | 4.242 |
| | 0.5 | 1 | 0.25 | 1.5478 | 4.144 | 5.839 | 11.73 | 13.302 |
| | 0.5 | 1 | 1 | 1.39 | 3.696 | 4.991 | 10.066 | 12.251 |
| | 0.5 | 1 | 4 | 1.238 | 3.32 | 4.177 | 7.774 | 10.107 |
| | 2 | 1 | 0.25 | 0.962 | 1.979 | 2.664 | 5.313 | 6.877 |
| | 2 | 1 | 1 | 0.893 | 1.799 | 2.345 | 4.58 | 5.976 |
| | 2 | 1 | 4 | 0.825 | 1.637 | 2.042 | 3.618 | 4.724 |
| $Re = 10$ | 1 | 0.5 | 0.25 | 4.4115 | 9.644 | 12.134 | 15.558 | 16.55 |
| | 1 | 0.5 | 1 | 1.713 | 4.351 | 6.0639 | 11.601 | 13.512 |
| | 1 | 0.5 | 4 | 0.29955 | 1.818 | 2.808 | 5.2452 | 7.0598 |
| | 1 | 1 | 0.25 | 1.5573 | 3.560 | 4.9651 | 9.4925 | 11.431 |
| | 1 | 1 | 1 | 1.4375 | 3.178 | 4.3246 | 8.4464 | 10.406 |
| | 1 | 1 | 4 | 1.305 | 2.792 | 3.5371 | 6.7391 | 8.6389 |
| | 1 | 2 | 0.25 | 2.1071 | 4.3082 | 5.8148 | 4.6509 | 11.611 |
| | 1 | 2 | 1 | 1.0646 | 2.1 | 2.7988 | 5.4724 | 7.0273 |
| | 1 | 2 | 4 | 0.28405 | 1.1061 | 1.4776 | 2.5441 | 3.3152 |
| | 0.5 | 1 | 0.25 | 2.8234 | 6.2717 | 8.4648 | 13.194 | 14.615 |
| | 0.5 | 1 | 1 | 2.6458 | 5.5148 | 7.478 | 12.259 | 13.819 |
| | 0.5 | 1 | 4 | 2.4604 | 4.5335 | 5.9291 | 10.59 | 12.401 |
| | 2 | 1 | 0.25 | 0.81017 | 2.0013 | 2.7556 | 5.8429 | 7.618 |
| | 2 | 1 | 1 | 0.73988 | 1.813 | 2.4298 | 5.0295 | 6.677 |
| | 2 | 1 | 4 | 0.66523 | 1.6055 | 2.0858 | 3.861 | 5.1864 |
| $Re = 100$ | 1 | 0.5 | 0.25 | 3.2954 | 7.5365 | 9.8892 | 14.268 | 15.493 |
| | 1 | 0.5 | 1 | 3.1013 | 6.905 | 9.3007 | 14.181 | 15.62 |
| | 1 | 0.5 | 4 | 2.7754 | 5.3926 | 7.3127 | 12.498 | 14.272 |
| | 1 | 1 | 0.25 | 1.8545 | 4.3319 | 6.08 | 10.862 | 12.74 |
| | 1 | 1 | 1 | 1.744 | 3.9119 | 5.51 | 10.351 | 12.395 |
| | 1 | 1 | 4 | 1.5226 | 3.0919 | 4.1069 | 8.0948 | 10.239 |
| | 1 | 2 | 0.25 | 0.9931 | 2.4054 | 3.3894 | 7.0204 | 8.971 |
| | 1 | 2 | 1 | 0.9237 | 2.2122 | 3.10428 | 6.444 | 8.3648 |
| | 1 | 2 | 4 | 0.8074 | 1.7825 | 2.2804 | 4.5486 | 6.0778 |
| | 0.5 | 1 | 0.25 | 2.3449 | 6.1041 | 8.6512 | 13.983 | 17.006 |
| | 0.5 | 1 | 1 | 2.3659 | 6.7248 | 9.9664 | 16.245 | 17.378 |
| | 0.5 | 1 | 4 | 1.74 | 3.8787 | 5.2024 | 10.143 | 12.853 |
| | 2 | 1 | 0.25 | 1.3048 | 2.7898 | 3.8469 | 7.373 | 12.715 |
| | 2 | 1 | 1 | 1.2512 | 2.5661 | 3.5201 | 6.8615 | 8.6874 |
| | 2 | 1 | 4 | 1.5226 | 3.0919 | 4.1069 | 8.0948 | 10.239 |

## 5. Conclusion & perspectives

In this paper, the hydrodynamic of a spherical droplet in a uniform flow has been investigated alongside with the conjugate mass transfer problem by means of direct numerical simulation. Simulation were performed for Reynolds numbers up to $Re = 100$ and relatively wide range of viscosity ratio $0.1 \leq \mu^* \leq 15$ for the hydrodynamic part, the validation step showed that our results are in perfect agreement with previous works so far and that a simple correlation of the drag coefficient might be used with a good precision. A simple correlation of the separation angle has been proposed as well. For mass transfer, three additional parameters (Diffusivity ratio, Henry coefficient and the Peclet number) whose effect on the Sherwood number has been analyzed. The objective of the present study is to shed the light on the complexity of the conjugate problem and the multi-parameters that impact highly the physics of the transfer. A non-trivial behaviour of the asymptotic Sherwood number has been detected when the problem is convective and the Henry coefficient/diffusivity ratio are small. Future work will be dedicated to finding an acceptable correlation of the Sherwood number and 3D simulation for hight Reynolds number.


## Acknowledgement

This work was supported by the Nuclear Energy Division of CEA (program SIACY). The authors acknowledge the COSINUS service at the IMFT for their technical support: Kevin LARNIER, Annaïg PEDRONO.


## Appendix A. Mesh parameters

$$d1v = \frac{d_2^2 - d_1^2}{d_1 d_2 (d_2 - d_1)} \tag{A.1}$$

$$d2v = \frac{d_2^2}{d_1 d_2 (d_2 - d_1)} \tag{A.2}$$

$$d3v = \frac{d_1^2}{d_1 d_2 (d_2 - d_1)} \tag{A.3}$$

$$d1v' = \frac{{d'_2}^2 - {d'_1}^2}{d'_1 d'_2 (d'_2 - d'_1)} \tag{A.4}$$

$$d2v' = \frac{{d'_2}^2}{d'_1 d'_2 (d'_2 - d'_1)} \tag{A.5}$$

$$d3v' = \frac{{d'_1}^2}{d'_1 d'_2 (d'_2 - d'_1)} \tag{A.6}$$

$$\tag{A.7}$$

## Appendix B. Correlations

For $0 \leq Re \leq 5$ [8]

$$C_D = \frac{8}{Re}\frac{3\mu^* + 2}{\mu^* + 1}\left(1 + 0.05\frac{3\mu^* + 2}{\mu^* + 1}Re\right) - 0.01\frac{3\mu^* + 2}{\mu^* + 1}Re\ln(Re) \tag{B.1}$$

For $5 < Re < 1000$ [8]

$$C_D(Re, \mu^*) = \begin{cases} \dfrac{2 - \mu^*}{2}C_D(Re, 0) + \dfrac{4\mu^*}{6 + \mu^*}C_D(Re, 2) & 0 \leq \mu^* \leq 2 \\ \dfrac{4}{\mu^* + 2}C_D(Re, 2) + \dfrac{\mu^* - 2}{\mu^* + 2}C_D(Re, \infty) & 2 < \mu^* \leq \infty \end{cases} \tag{B.2}$$

where

$$\begin{cases} C_D(Re, 0) = \dfrac{48}{Re}\left(1 - \dfrac{2.21}{\sqrt{Re}} + \dfrac{2.14}{Re}\right) \\ C_D(Re, 2) = 17.0Re^{2/3} \\ C_D(Re, \infty) = \dfrac{24}{Re}\left(1 + \dfrac{1}{6}Re^{2/3}\right) \end{cases} \tag{B.3}$$

Drag coefficients of particle/bubble :

$$\begin{cases} {C_D}^{particle} = \dfrac{24}{Re}\left(1. + 0.15Re^{0.687}\right) & Re \leq 800 \quad \text{[Schiller \& Nauman]} \\ {C_D}^{bubble} = \dfrac{16}{Re}\left[1 + \left(\dfrac{8}{Re} + 0.5\left(1 + 3.315Re^{-0.5}\right)\right)^{-1}\right] & 0.1 \leq Re \leq 200 \quad \text{[Mei \& Klausner]} \end{cases} \tag{B.4}$$

## References


[1] B Abramzon and C Elata. Unsteady heat transfer from a single sphere in stokes flow. *International journal of heat and mass transfer*, 27(5):687–695, 1984.

[2] BM Abramzon and GA Fishbein. Some problems of convective diffusion to a spherical particle with $pe \leq 1000$. *Journal of engineering physics*, 32(6):682–686, 1977.

[3] Silvia Alexandrova, Maria Karsheva, Abdellah Saboni, and Christophe Gourdon. Effect of the viscosity ratio on the mass transfer into a spherical drop in liquid-liquid dispersions. *Journal of Chemical Technology and Metallurgy*, 49(5):429–434, 2014.

[4] AS Brignell. Solute extraction from an internally circulating spherical liquid drop. *International Journal of Heat and Mass Transfer*, 18(1):61–68, 1975.

[5] R Clift, JR Grace, and ME Weber. Bubbles, drops, and particles. 1978.

[6] Damien Colombet, Dominique Legendre, Arnaud Cockx, and Pascal Guiraud. Mass or heat transfer inside a spherical gas bubble at low to moderate reynolds number. *International Journal of Heat and Mass Transfer*, 67:1096–1105, 2013.

[7] Fred Cooper. Heat transfer from a sphere to an infinite medium. *International Journal of Heat and Mass Transfer*, 20(9):991–993, 1977.

[8] Zhi-Gang Feng and Efstathios E Michaelides. Drag coefficients of viscous spheres at intermediate and high reynolds numbers. *Journal of Fluids Engineering*, 123(4):841–849, 2001.

[9] Zhi-Gang Feng and Efstathios E Michaelides. Heat and mass transfer coefficients of viscous spheres. *International journal of heat and mass transfer*, 44(23):4445–4454, 2001.

[10] Bruce A Finlayson. *The method of weighted residuals and variational principles*, volume 73. SIAM, 2013.

[11] LE Johns and RB Beckmann. Mechanism of dispersed-phase mass transfer in viscous, single-drop extraction systems. *AIChE Journal*, 12(1):10–16, 1966.

[12] Gh Juncu. Unsteady heat and/or mass transfer from a fluid sphere in creeping flow. *International journal of heat and mass transfer*, 44(12):2239–2246, 2001.

[13] Gheorghe Juncu. Unsteady ternary mass transfer from a sphere in creeping flow. *International journal of thermal sciences*, 44(3):255–266, 2005.

[14] Gheorghe Juncu. A numerical study of the unsteady heat/mass transfer inside a circulating sphere. *International Journal of Heat and Mass Transfer*, 53(15-16):3006–3012, 2010.

[15] Leonid S Kleinman and XB Reed. Unsteady conjugate mass transfer between a single droplet and an ambient flow with external chemical reaction. *Industrial & engineering chemistry research*, 35(9): 2875–2888, 1996.

[16] R Kronig and JC Brink. On the theory of extraction from falling droplets. *Applied Scientific Research*, 2(1):142, 1951.

[17] A Kumar and S Hartland. Correlations for prediction of mass transfer coefficients in single drop systems and liquid–liquid extraction columns. *Chemical Engineering Research and Design*, 77(5):372–384, 1999.

[18] Jacques Magnaudet, Mayela Rivero, and Jean Fabre. Accelerated flows past a rigid sphere or a spherical bubble. part 1. steady straining flow. *Journal of fluid mechanics*, 284:97–135, 1995.

[19] Renwei Mei and James F Klausner. Unsteady force on a spherical bubble at finite reynolds number with small fluctuations in the free-stream velocity. *Physics of Fluids A: Fluid Dynamics*, 4(1):63–70, 1992.

[20] Albert Broadus Newman. The drying of porous solids: diffusion and surface emission equations. *AIChE Trans.*, 27:203–220, 1931.

[21] DLR Oliver and JN Chung. Flow about a fluid sphere at low to moderate reynolds numbers. *Journal of Fluid Mechanics*, 177:1–18, 1987.

[22] DLR Oliver and JN Chung. Unsteady conjugate heat transfer from a translating fluid sphere at moderate reynolds numbers. *International Journal of Heat and Mass Transfer*, 33(3):401–408, 1990.

[23] Douglas LR Oliver and Jacob N Chung. Conjugate unsteady heat transfer from a spherical droplet at low reynolds numbers. *International journal of heat and mass transfer*, 29(6):879–887, 1986.

[24] AR Paschedag, WH Piarah, and M Kraume. Sensitivity study for the mass transfer at a single droplet. *International journal of heat and mass transfer*, 48(16):3402–3410, 2005.

[25] SB Pope. The calculation of turbulent recirculating flows in general orthogonal coordinates. *Journal of Computational Physics*, 26(2):197–217, 1978.

[26] Mayela Rivero. *Etude par simulation numérique des forces exercées sur une inclusion sphérique par un écoulement accéléré*. PhD thesis, Toulouse, INPT, 1991.

[27] Eli Ruckenstein. Mass transfer between a single drop and a continuous phase. *International Journal of Heat and Mass Transfer*, 10(12):1785–1792, 1967.

[28] Abdellah Saboni, Silvia Alexandrova, Maria Karsheva, and Christophe Gourdon. Mass transfer from a contaminated fluid sphere. *AIChE Journal*, 57(7):1684–1692, 2011.

[29] Sebastian Ubal, CH Harrison, P Grassia, and WJ Korchinsky. Numerical simulation of mass transfer in circulating drops. *Chemical Engineering Science*, 65(10):2934–2956, 2010.

[30] AR Uribe-Ramirez and WJ Korchinsky. Fundamental theory for prediction of multicomponent mass transfer in single-liquid drops at intermediate reynolds numbers ($10 \leq re \leq 250$). *Chemical engineering science*, 55(16):3319–3328, 2000.

[31] M Wegener, N Paul, and M Kraume. Fluid dynamics and mass transfer at single droplets in liquid/liquid systems. *International Journal of Heat and Mass Transfer*, 71:475–495, 2014.

[32] Christophe Wylock, Pierre Colinet, and Benoit Haut. Gas absorption into a spherical liquid droplet: numerical and theoretical study. *Chemical engineering journal*, 207:851–864, 2012.